

Competing charge density wave phases in YNiC_2

Marta Roman,^{1,2,*} Simone Di Cataldo,^{1,3} Berthold Stöger,⁴ Lisa Reisinger,¹ Emilie Morineau,¹ Kamil K. Kolincio,⁵ and Herwig Michor^{1,†}

¹*Institute of Solid State Physics, TU Wien, Wiedner Hauptstrasse 8-10, A-1040 Wien, Austria*

²*Institute of Physics and Applied Computer Science, Faculty of Applied Physics and Mathematics, Gdansk University of Technology, Narutowicza 11/12, 80-233 Gdansk, Poland*

³*Dipartimento di Fisica, Sapienza University of Rome, Piazzale Aldo Moro 5, 00185 Rome, Italy*

⁴*X-Ray Center, TU Wien, Getreidemarkt 9, A-1060 Wien, Austria*

⁵*Faculty of Applied Physics and Mathematics, Gdansk University of Technology, Narutowicza 11/12, 80-233 Gdansk, Poland*

Charge density wave (CDW) orders in YNiC_2 are studied by means of combined experimental and computational techniques. On the experimental side, single crystals grown by the floating-zone method were examined by means of X-ray diffraction, as well as transport and thermal techniques. Density functional theory (DFT) calculations founded on the experimentally determined parent and CDW-modified crystal structures provide details of electronic and phononic structures as well as electron-phonon coupling and resolve changes inflicted upon entering the different CDW phases. Thereby, contrasting effects of subsequently emerging CDW states characterized by incommensurate q_{1c} and commensurate q_{2c} modulation vectors are revealed. The former state, on-setting below $T_{1c} \simeq 305$ K, weakly modifies the electronic structure by opening an almost isotropic gap on a minor part of the Fermi surface (FS). The latter phase, which takes over below $T_{2c} \simeq 272$ K has a more pronounced impact on physical properties via a decomposition of larger parts of the FS. These dissimilar behaviors are directly reflected in the electronic transport anisotropy, which is significantly weakened in the q_{2c} -type CDW state. As revealed by our DFT studies, CDW phases are very close in energy and their origin is directly related to the anisotropy of electron-phonon coupling, which is linked to a specific orbital character of related FS sheets. Specific heat and thermal expansion studies reveal a nearly reversible first-order phase transition at around $T_{2c} \simeq 272$ K, where both CDW phases co-exist within a T -interval of about 10 K.

I. INTRODUCTION

Electron-electron and electron-phonon couplings give rise to a broad horizon of physical phenomena, including superconductivity, and spin- or charge density waves. The presence of multiple coexisting, intertwined or competing charge density waves (CDW) is typically associated with a geometry of the Fermi surface (FS) that enables multiple electronic instabilities, or with a strongly momentum-dependent electron-phonon coupling [1–3]. While the former, geometric term prevails in systems with an essentially 1D electronic structure, giving rise to nesting-susceptible planar FS sheets, the latter plays a more decisive role in real systems with higher dimensionality [4–7].

The coexistence or competition of distinct CDW instabilities has been observed in various systems, including transition metal dichalcogenides [8–10], bronzes [11], rare-earth tellurides [12–15], or recently, in metals with kagome-lattice crystal structure [16–18]. In extreme cases, when the presence of such multiple degrees of freedom brings two states close in the scale of free energy, a small imbalance, driven by external factors such as light, may become sufficient to open a non-equilibrium state corresponding to another local energy minimum [19].

An abundant sandbox for exploring interactions be-

tween various types of order parameters is provided by rare-earth nickel dicarbides $R\text{NiC}_2$ – a class of materials known for a rich phase diagram comprising CDW phases, various magnetic states and superconductivity, systematically evolving with the lanthanide contraction [20–26]. Their electronic structure with quasi-one-dimensional character creates favorable conditions for CDW formation, in some cases with multiple CDW transitions. In $R\text{NiC}_2$ compounds ($R = \text{Pr} - \text{Sm}$) with larger unit-cell volume, CDW superstructures are characterized by a single incommensurate $q_{1c} = (0.5, 0.5 + \delta, 0)$ modulation wave vector, which may finally lock-in to a commensurate modulation $q_{1c} = (0.5, 0.5, 0)$ at low temperature as reported for GdNiC_2 [20–22]. Upon replacing the rare-earth with heavier R -elements, one observes the emergence and eventually a prevalence of CDW order characterized by a commensurate modulation vector $q_{2c} = (0.5, 0.5, 0.5)$ [24–26]. YNiC_2 hosts both, the incommensurate q_{1c} -type and the commensurate q_{2c} -type CDW states [24]. Despite the observed signatures, the driving forces governing these two electronic instabilities have not been identified and explored yet.

Here we report on single-crystal studies of YNiC_2 , via X-ray diffraction, thermodynamic and anisotropic transport measurements, aiming to explore the CDW phases and their crossover from the q_{1c} -type CDW state to the q_{2c} -type CDW ground state phase. Experimental studies are complemented by density functional theory (DFT) calculations of electronic and vibrational properties to investigate the driving forces of CDW formation in this

* marta.roman@pg.edu.pl

† michor@ifp.tuwien.ac.at

material.

II. EXPERIMENTAL

The polycrystalline material, needed to grow a single crystal, has been synthesized using radio-frequency induction technique in a high-purity argon atmosphere (99.9999%). Pure elements: Y (99.9%), Ni (99.99%) metals, and carbon (graphite, 99.999%) have been used as precursors in this procedure. In a next step, polycrystalline feed and seed rods were prepared, using the same induction melting method, and then used to grow monocrystalline YNiC_2 via the floating zone technique in an optical mirror furnace (Crystal Systems Corporation, Japan). Single crystals were finally oriented by means of the Laue method and cut along the principal orientations of the orthorhombic parent structure, in dimensions as desired for specific measurements.

An initial characterization of the YNiC_2 crystal was performed via scanning electron microscopy (SEM) using a Philips XL30 ESEM with EDAX XL-30 EDX detector and powder X-ray diffraction (pXRD) with an *Aeris* powder diffractometer by Malvern Panalytical. A homogeneous 1-1-2 stoichiometry with no relevant inclusions of impurities was confirmed by electron microprobe studies and is well supported by pXRD data.

Single crystal diffraction data of small fragments of YNiC_2 were collected on a *STOE Stadivari* diffractometer system [27] equipped with a *Dectris EIGER* CdTe hybrid phonon counting detector using $\text{MoK}\alpha$ radiation in a dry stream of nitrogen in the 250 to 300 K range. Data were processed using the *X-Area* software package and a correction for absorption effects applied using the multi-scan approach implemented in *LANA* [27]. The low-temperature (LT) commensurate CDW phase was treated as a twin of index 2 ('HKLF5' style reflection data). Initial models were generated using the coordinates of the isotypic LuNiC_2 structures [26]. The structures were refined against F^2 using *Jana2006* [28]. All atoms were refined with anisotropic displacement parameters (ADPs). In the twinned LT phase the ADPs of the two C and the two distinct Y atoms were constrained to be equal up to the $2_{[001]}$ operation of the high-temperature phase. The correct orientation of all domains was unambiguously established based on the Flack parameter. Data collection and refinement details are compiled in Table I. Further details on the crystal structure analyses of the triperiodic structure can be obtained from the inorganic crystal structure database (ICSD) [29] on quoting the depository listed at the end of Table I.

To study thermal expansion above room temperature, pXRD patterns were collected from 300 to 380 K using a Panalytical X'Pert Pro diffractometer equipped with an Anton-Paar HTK-1200 chamber with He atmosphere. Low-temperature thermal expansion (4.3–310 K) was measured by capacitive dilatometry employing a tilted plate geometry [30]. The size of the cuboid-like oriented

YNiC_2 crystal used for heat capacity and LT thermal expansion studies was $1.46 \times 2.28 \times 1.24 \simeq 4.13 \text{ mm}^3$.

Heat capacity measurements from 2 to 380 K were carried out on a commercial Quantum Design, Physical Properties Measurement System (PPMS) employing a relaxation-type method. Apiezon-H grease was applied for measurements above 300 K, while Apiezon-N was used as thermal contact medium at below 310 K.

A conventional four-probe technique was used for the electrical resistivity measurements in a PPMS system. Thin ($\phi = 50 \mu\text{m}$) gold wires serving as electrical contacts were spark welded to the polished surface of bar-shaped single crystals with typical dimensions $\sim 3 \times 1 \times 0.5 \text{ mm}^3$ cut along the principal orthorhombic orientations.

DFT calculations were performed using Quantum ESPRESSO [31, 32]. We employed optimized norm-conserving Vanderbilt pseudo-potentials [33], with the Perdew-Burke-Ernzerhof exchange-correlation functional. Kohn-Sham wavefunctions were expanded in a plane waves basis set using a kinetic energy cutoff of 80 Ry. For calculations of the orthorhombic and q_{2c} -type CDW we employed the experimental crystal structures, while the q_{1c} -type structure was described using a 16-atoms commensurate approximant. Due to the varying cell size, we employed different meshes for Brillouin zone integration for the parent, q_{1c} -type and q_{2c} -type unit cells, as detailed in Sect. I of the Supplemental Material (SM) [34]. Densities of states, band structures, and Fermi surfaces were computed non-self-consistently on finer grids as detailed in SM [34] Sect. I. The latter were visualized using *Fermisurfer* [40].

Phonon calculations were performed using density functional perturbation theory, as implemented in Quantum ESPRESSO, and interpolated using Wannier functions using EPW [41, 42] to obtain the phonon frequencies and linewidths from the real and imaginary part of the selfenergy (for further details including the wannierization windows, see SM [34] Sect. II).

The special points for band structures and phonon dispersions for the parent phase are defined according to Ref. [35]: $\Gamma = (0.00, 0.00, 0.00)$; $S = (0.00, 0.50, 0.00)$; $R = (0.00, 0.50, 0.50)$; $Z = (0.00, 0.00, 0.50)$; $T = (-0.50, 0.50, 0.50)$; $Y = (-0.50, 0.50, 0.00)$; $\Sigma_0 = (0.39, 0.39, 0.00)$; $A_0 = (0.39, 0.39, 0.50)$ (see Fig. 7a). The details on how we obtained the corresponding points for the q_{1c} - and q_{2c} -type CDW cells are given in SM [34] Sect. II.

III. RESULTS AND DISCUSSION

A. Crystal structures

Like all members of the $R\text{NiC}_2$ family at elevated temperatures, YNiC_2 also crystallize in the orthorhombic *Amm2* aristotype structure (Fig. 1a) [44]. All metal atoms and the C_2 dumbbells are located on sites with *mm2* symmetry. The Ni atoms and the C_2 dumbbells are

TABLE I. Data collection and refinement details of the incommensurately modulated and triperiodic CDW phases of YNiC₂. R - and $wR2$ -values of the incommensurate structure at 280 K refer to refinements of all reflections, main reflections and 1st order satellites, respectively.

T (K)	320	280	250
M	171.6	171.6	171.6
Space group	$Amm2$	$Amm2(\frac{1}{2}\sigma_20)000$	Cm
a (Å)	3.5724 (2)	3.5699 (5)	7.5223 (7)
b (Å)	4.5069 (3)	4.5062 (6)	7.1387 (6)
c (Å)	6.0321 (5)	6.0267 (9)	3.7635 (4)
β (deg.)	90	90	106.498 (7)
V (Å ³)	97.120 (12)	96.95 (2)	193.78 (3)
Z	2	2	4
D_{calcd} (g cm ⁻¹)	5.869	5.879	5.883
μ (mm ⁻¹)	38.907	38.975	38.999
Crystal size (μ m ³)	$50 \times 28 \times 5$	$90 \times 77 \times 60$	$60 \times 37 \times 20$
θ_{max}	41.21	45.28	41.09
Reflections			
measured	2780	2780	8226
unique main	378	467	1659
1 st order satellites	–	794	
observed ($I > 2\sigma(I)$)	377	467	960
1 st order satellites	–	469	
Parameters	17	22	32
R_{int}	0.0236	0.0298	0.0524
R ($I > 2\sigma(I)$)	0.0159	0.0536, 0.0502, 0.0844	0.0431
$wR2$ (all)	0.0400	0.1379, 0.1275, 0.1813	0.1116
GooF	1.73	1.78	1.18
Extinction (Gaussian)	180 (15)	160 (40)	138 (17)
Diff. el. density			
min, max (e Å ⁻³)	–0.44, 0.67	–1.79, 2.01	–3.62, 2.70
Twin operation	–	–	$2_{[102]}$
Twin volume fraction	–	–	73.2:26.8 (4)
CSD Number	2392983	–	2392982

located on the $x = 0$ planes, the Y atoms on the $x = \frac{1}{2}$ planes. The Ni and Y atoms form linear chains extending along [100], whereby adjacent atoms are related by the

TABLE II. Atomic coordinates and modulation functions in the q_{1ic} incommensurately modulated CDW phase of YNiC₂.

M	x	0
	y	$-0.00591(7) \sin(2\pi\bar{x}_4)$
	z	$0.38848(3) - 0.00219(7) \cos(2\pi\bar{x}_4)$
Ni	x	$\frac{1}{2} + 0.01399(13) \sin(2\pi\bar{x}_4)$
	y	0
	z	0.00000(6)
C	x	$\frac{1}{2} + 0.0049(7) \cos(2\pi\bar{x}_4) - 0.0007(6) \sin(2\pi\bar{x}_4)$
	y	0.3494(7)
	z	0.1886(5)

a lattice translation with interatomic distances at 320 K, $a = 3.5724$ (2) Å.

Figure 2a sketches the temperature dependent evolution of structural phases. Below T_{2c} , YNiC₂ crystallizes as twofold monoclinic Cm superstructure [$\mathbf{q}_{2c} = \frac{1}{2}(\mathbf{a}^* + \mathbf{b}^* + \mathbf{c}^*)$ modulation of the orthorhombic parent structure], which is isotypic with the corresponding LuNiC₂ and TmNiC₂ structures. The lost point group operations are retained as twin operations (see Table I). The structure is characterized by formation of Ni–Ni Peierls pairs in rods extending along [100] with short distances of 3.4351 (9) Å which alternate with long distances of 3.7036 (9) Å at 250 K. A detailed description of the monoclinic structure type has been given previously [25, 26].

Between T_{1ic} and T_{2c} , YNiC₂ adopts a 1D (along the orthorhombic b -axis) incommensurately modulated structure analogous to SmNiC₂ [45] with superspace group symmetry $Amm2(\frac{1}{2}\sigma_20)000$, and modulation wave

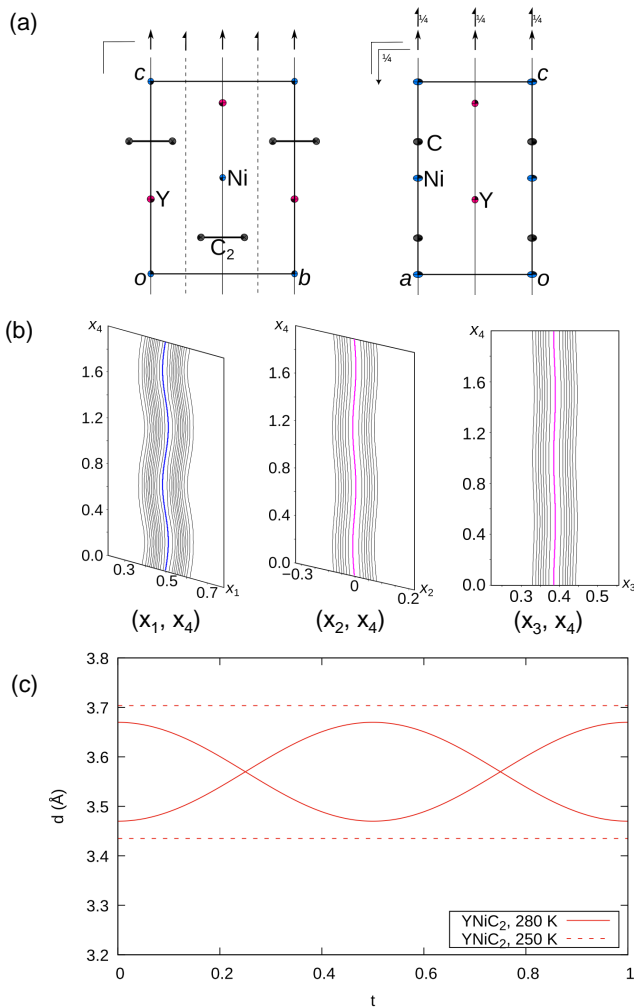


FIG. 1. (a) The crystal structure of the orthorhombic $Amm2$ aristotype phase of $YNiC_2$ viewed along (left) $[100]$ and (right) $[010]$. Y (magenta), Ni (blue) and C (grey) atoms are represented by ellipsoids drawn at the 75% probability levels. Symmetry elements are indicated using the usual graphical symbols [43]. (b) Sections through the superspace of $YNiC_2$ centered around the (left) Ni and (middle, right) Y atoms in the basic structure. The barycenters of the atoms are indicated by blue (Ni) and magenta (Y) curves. Contours are drawn at the (a) 20 and (b) 50 $e^- \text{Å}^{-3}$ levels. (c) t -plot of the Ni—Ni-distances in $[100]$ direction in the incommensurately modulated phases of $YNiC_2$ red solid line. There are two lines for each case, as each row of Ni atoms extending in the $[100]$ direction alternates between short and long distances (except for $t = 0, \frac{1}{2}$, where Ni atoms are equidistant as in the aristotype structure). For reference, the corresponding distances in the commensurate Cm structures are indicated by dashed lines.

vector $\mathbf{q}_{1ic} = \frac{1}{2}\mathbf{a}^* + \sigma_2\mathbf{b}^*$ with $\sigma_2 = 0.5138(8)$ at 280 K. Accordingly, periodicity in the $[100]$ direction is halved (doubling of the a -axis, as in the monoclinic Cm structures) fully retained in the $[001]$ direction and lost in $[010]$ direction. For single crystal XRD data taken right

at 275 K, *i.e.* in the vicinity of T_{2c} , satellite reflections related to both modulation wave vectors q_{2c} and q_{1ic} are observed and attributed to a coexistence of q_{2c} - and q_{1ic} -type CDW domains (see Sect. III C for a discussion on details of the related phase transition and Fig. S1 in SM [34], for the diffraction image).

Since the basic structures of the incommensurate phases are isotypic to the aristotype phases, comparable atomic coordinates were used, up to the x -coordinates, which were shifted by $\frac{1}{2}$. The $Amm2$ basic structure contains two symmetrically equivalent reflection planes parallel to (100) (see Fig. 1a) and the origin may be chosen on either of the planes. In the $Amm2(\frac{1}{2}\sigma_2 0)000$ superspace group, these reflection planes split in two distinct symmetry elements. The $x = 0$ plane remains a proper mirror plane in the modulated structure. In contrast, reflecting at $x = \frac{1}{2}$ shifts the modulation functions by half a period, which can be regarded as the incommensurate equivalent of a glide reflection. If the x -coordinates of the basic structure were retained (Ni at $x = 0$), the Ni atoms could not be displaced in the $[100]$ direction. The resulting model gives refinements with excellent reliability factors, but is unlikely, given the Peierls pair formation in the commensurate Cm structures. Note that an analogous phenomenon is observed in the commensurate LT phase: The reflection planes parallel to (100) of the aristotype structure split into an alternation of proper reflection planes and glide reflection planes with an intrinsic translation component of $\frac{1}{2}(\mathbf{b} + \mathbf{c})$ [25]. There as well, the Ni atoms had to be moved to $x = \frac{1}{2}$.

The displacement modulation of all atoms was described by first-order harmonics (see Table II). No discontinuity was apparent in the modulation functions (Fig. 1b). Since the Y atoms are located on the $x = 0$ reflection plane, displacement is only possible parallel to the (100) plane. For symmetry constraints, first-order harmonic modulation waves only allow modulation in the $[100]$ direction for the Ni atoms and the C atoms. Theoretically, second-order harmonics could allow for an additional displacement in the (100) plane, but these components refined to zero within experimental error.

The following discussion of the modulation will focus on the Ni atoms, which are the crucial point of the CDW formation. The position of the Ni atom located at $\bar{\mathbf{x}}$ in the basic structure is given as

$$x_1 = \bar{\mathbf{x}} + [\Delta x \sin(2\pi\bar{\mathbf{x}} \cdot \mathbf{q})]\mathbf{a}, \quad (1)$$

where Δx is the sine-component of the Ni displacement modulation wave listed in Table II and assuming that the modulation phase t equals 0 for brevity. Since the σ_1 -component of the \mathbf{q} -vector is $\frac{1}{2}$, the Ni atom translated by an \mathbf{a} lattice translation in the basic structure is located at

$$\begin{aligned} x_2 &= \bar{\mathbf{x}} + \mathbf{a} + \left\{ \Delta x \sin\left[2\pi\left(\bar{\mathbf{x}} \cdot \mathbf{q} + \frac{1}{2}\right)\right] \right\} \mathbf{a} \\ &= \bar{\mathbf{x}} + [1 - \Delta x \sin(2\pi\bar{\mathbf{x}} \cdot \mathbf{q})]\mathbf{a} \end{aligned} \quad (2)$$

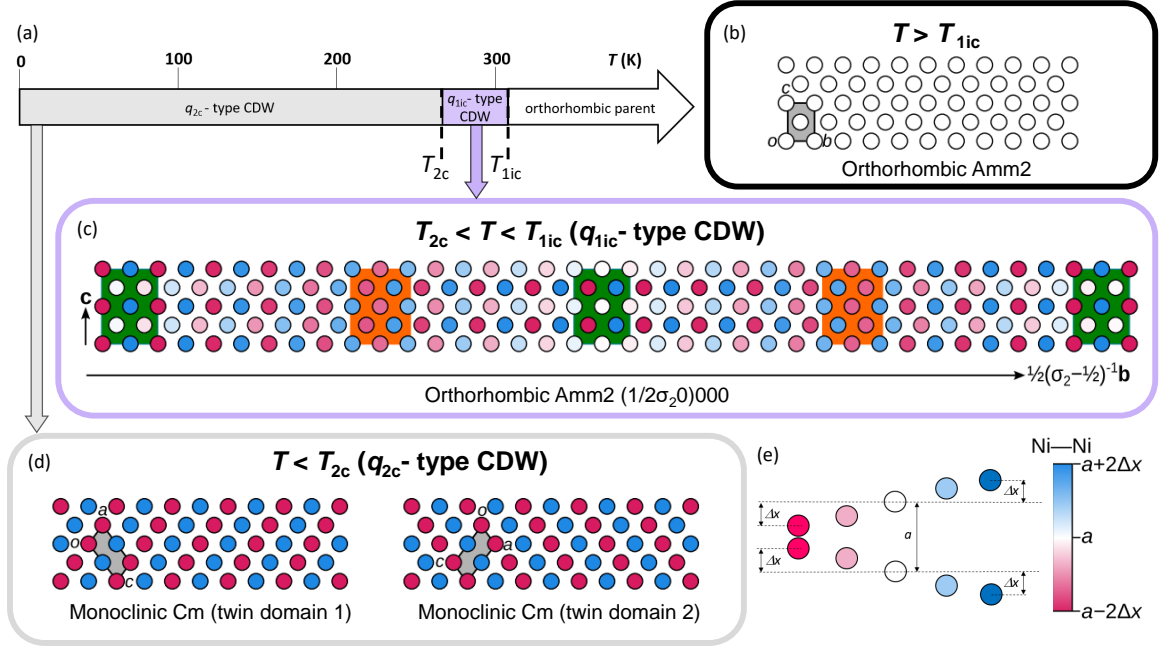


FIG. 2. (a) Phase evolution as function of temperature in YNiC_2 compound. (b) - (d) Schematic representation of Ni—Ni-distances in a (100) section of: (b) the $Amm2$ aristotype structure, (c) the incommensurately modulated CDW structure, viewed in $[100]$ direction and (d) both twin domains of the Cm commensurate CDW structures. In panels (b) - (d), the Ni—Ni pairs are represented by disks, and their colors represent the relevant Ni—Ni distance as graphically explained in panel (e); white marks the average value ($= a$ lattice parameter of the parent structure), dark blue and pink colors represent the pairs with longest and shortest Ni—Ni distances, respectively. Y atoms and C_2 dumbbells are omitted for clarity.

By subtraction of Eqns. 1 and 2, one notes that in the $[100]$ direction, Ni atoms are arranged in lines spaced alternately by

$$x_1 - x_2 = [1 \pm 2\Delta x \sin(2\pi\bar{\mathbf{x}} \cdot \mathbf{q})]a, \quad (3)$$

which corresponds to the Peierls pairs also observed in the commensurate Cm phases. Here however, the amplitude of the Peierls pair formation varies across the structure. Since the modulation functions are continuous, each Ni—Ni-distance in the $a - 2\Delta x$ to $a + 2\Delta x$ range is realized. In particular, rods where the Ni—Ni distances are a correspond to the $Amm2$ aristotype structure with equidistant Ni atoms.

Figure 1c shows a t -plot of the Ni—Ni distances in YNiC_2 . At its maximum, Peierls pair formation is slightly less pronounced than in the commensurate LT phase. A translation by \mathbf{b} in the basic structure corresponds to a t -shift by $\sigma_2 \approx 0.514$, *i.e.* short Ni—Ni distances follow long Ni—Ni distances and vice-versa. Moreover, intermediate Ni—Ni distances are followed by intermediate Ni—Ni distances. Figure 2b–d shows schematic representations of structural phases with color-coded Ni—Ni distances in a plane parallel to (100). The color-code is graphically explained in Fig. 2e. The small deviation of σ_2 from $\frac{1}{2}$ results in a long modulation wave. Since the t -plot in Fig. 1c is symmetric by $t' = t + \frac{1}{2}$, the

modulation wave repeats after $2/0.014 \approx 36$ unit cells of the basic structure (see horizontal arrow in Fig. 2c).

The lattice translation $\frac{1}{2}(\mathbf{b} + \mathbf{c})$ of the $Amm2$ basic structure increases t by $\frac{1}{4} + \frac{\sigma_2}{2} \approx \frac{1}{4}$. Thus, rods with pronounced Peierls pairs are interleaved by rods with virtually no Peierls pair formation (green background in Fig. 2c, $t \approx \frac{n}{4}$, $n \in \mathbb{Z}$ in Fig. 1c). In contrast, rods with medium Peierls pairs combine with other rods of such Peierls pairs (orange background in Fig. 2c, $t \approx \frac{2n+1}{8}$, $n \in \mathbb{Z}$ in Fig. 1c). A putative lock-in phase with $\mathbf{q} = \frac{1}{2}(\mathbf{a}^* + \mathbf{b}^*)$ could be either of these two extremes.

B. Electrical resistivity studies

A charge density wave is essentially a coupled lattice and electronic instability, typically associated with the opening of one or more gaps at the Fermi energy. The evolution of the electronic component is directly reflected in the charge transport properties, which can be explored by macroscopic observables, such as the temperature-dependent electrical resistivity, $\rho(T)$. The latter, *i.e.* ρ_a , ρ_b , ρ_c , measured for single crystalline YNiC_2 with applied current along principal orientations is displayed in Fig. 3a and reveals distinct anomalies related to the two CDW

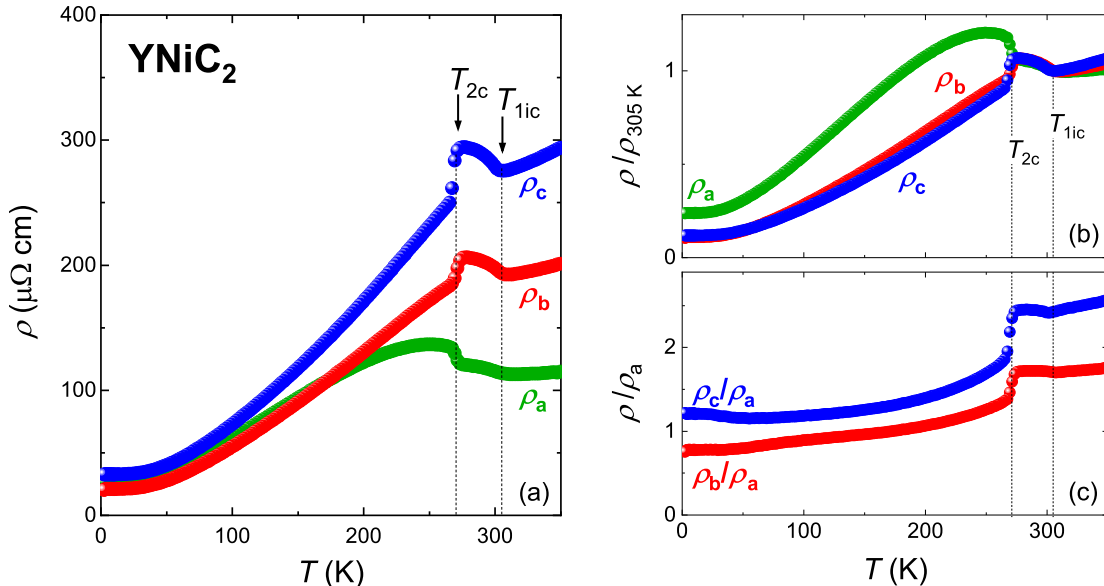


FIG. 3. (a) Temperature-dependent electrical resistivity, $\rho(T)$, measured on bar-shape YNiC_2 single crystals which were cut along orthorhombic a -, b - and c -orientations; (b) normalized electrical resistivity $\rho(T)/\rho(T_{1ic})$; (c) temperature-dependent relative anisotropy of the electrical resistivity ρ_b/ρ_a and ρ_c/ρ_a .

transitions discussed in Sect. III A. The first transition at $T_{1ic} = 305$ K (i) from the orthorhombic CeNiC_2 -type parent structure to the orthorhombic incommensurate q_{1ic} -type CDW and the second transition at $T_{2c} = 272$ K (ii) into a monoclinic commensurate q_{2c} -type CDW phase are well reflected by characteristic anomalies of the electrical resistivity, kink-like at T_{1ic} and jump-like at T_{2c} , respectively.

At temperatures above T_{1ic} , $\rho(T)$ data of YNiC_2 in Fig. 3a share the features of an anisotropic electrical resistivity $\rho_c > \rho_b > \rho_a$ as earlier reported for other $R\text{NiC}_2$ compounds in their CeNiC_2 -type parent state [21, 22, 25, 26]. At transition (i), a clear minimum at T_{1ic} followed by a $\rho(T)$ increase upon lowering the temperature, is observed for all three orthorhombic orientations (compare normalized resistivity data in Fig. 3b and relative anisotropy data in Fig. 3c), thus, revealing an almost unchanged anisotropy of ρ_a vs. ρ_b vs. ρ_c across T_{1ic} . The latter is a characteristic feature of the second-order phase transition into the q_{1ic} -type CDW state as previously reported for other $R\text{NiC}_2$ ($R = \text{Sm}, \text{Gd}, \text{Tb}$) representatives exhibiting this specific q_{1ic} -type CDW transition with a preserved orthorhombic point group symmetry [21, 22].

The transition (ii) from the q_{1ic} -type into the commensurate q_{2c} -type CDW state at T_{2c} is manifested by jump-like anomalies of all three $\rho(T)$ curves in Fig. 3a, *i.e.* by visible inflections seen simultaneously, yet clearly different for the different orientations. While $\rho_b(T)$ and $\rho_c(T)$

show a sharp downturn, the resistivity measured along the a direction, previously weakly affected at T_{1ic} , now visibly increases upon lowering the temperature. The pronounced anomaly of $\rho_a(T)$ accompanying the CDW crossover into the q_{2c} -type CDW state is not a sole domain of YNiC_2 , but appears to be a characteristic feature for this type of CDW order. Similarly specific response of $\rho_a(T)$ has been previously observed for single-crystalline TmNiC_2 and LuNiC_2 with a single CDW transition directly to the q_{2c} -type CDW state [25, 26]. With further decrease of temperature, the electrical resistivity gradually decreases for all three orientations. Within 100–200 K, a visible change of electronic anisotropy takes place with both ρ_b/ρ_a and ρ_c/ρ_a ratios gradually decreasing and saturating closer to unity as T is lowered (see Fig. 3c). A rather weak anisotropy of the electrical resistivity remains at lowest temperatures, with the lowest value for ρ_b , similar to earlier reported data of TmNiC_2 and LuNiC_2 [25, 26]. The residual resistivity of YNiC_2 , as measured at 2 K, is $\rho_{a0} = 27 \mu\Omega\text{cm}$, $\rho_{b0} = 20 \mu\Omega\text{cm}$, $\rho_{c0} = 33 \mu\Omega\text{cm}$.

Motivated by a previous transport study of polycrystalline YNiC_2 , which revealed the presence of a finite thermal hysteresis opening approximately at 285 K and closing at 265 K [39], we have investigated the character of both CDW anomalies in our single crystal via an electrical resistivity measurement with specific care on an optimal temperature stabilization (see SM [34], Sect. III for further details). The corresponding $\rho_c(T)$ measure-

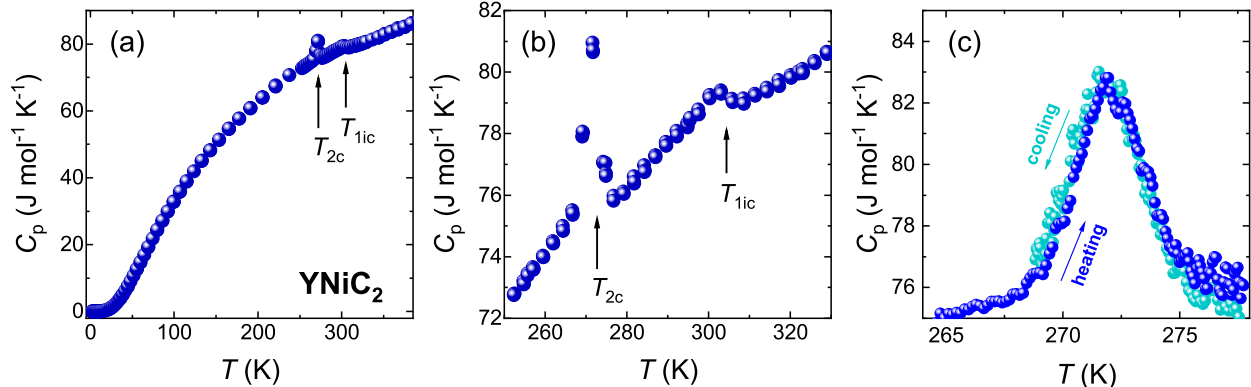


FIG. 4. (a) Temperature-dependent specific heat of single-crystalline YNiC_2 where CDW phase transitions are marked by black arrows. (b) Expanded view on both CDW phase transitions. (c) Specific heat anomaly related to the first order CDW transition at T_{2c} as determined via a slope analysis of heating (dark blue) and cooling (light blue) curves (see text).

ment (see Fig. S2 in SM [34]) clearly confirms thermal reversibility of the electrical resistivity upon heating and cooling across the second order transition (i) at T_{1ic} and reveals very narrow, but nonetheless finite thermal hysteresis of about 0.1 K for the anomaly at around T_{2c} . From the double-peak-like character of the temperature derivative of $\rho(T)$, we determine the width of transition (ii) ranging from about 265 to 275 K (see Fig. S3a in SM [34]). Accordingly, the width of the transition (~ 10 K) reveals to be two orders of magnitude larger than the width of the thermal hysteresis (~ 0.1 K) and the transition is thus almost perfectly reversible.

C. Specific heat and thermal expansion studies

Closer insight onto the nature of CDW phase transitions in YNiC_2 is revealed by specific heat and thermal expansion studies of YNiC_2 single crystals. The two CDW phase transitions identified by the above XRD and electrical resistivity studies are well reflected by corresponding anomalies of the temperature-dependent specific heat, $C_p(T)$, and thermal expansion, $\Delta l/l(T)$, measurements presented in Figs. 4 and 5, respectively. Most striking, apart from specific characteristics of the CDW transitions, is the overall strongly anisotropic behavior of the thermal expansion in Fig. 5a, which exhibits the largest expansion along the conventional orthorhombic a - and the smallest along the c -axis, *i.e.* YNiC_2 shows qualitatively a very similar behavior as earlier reported for TmNiC_2 [25].

Focusing on the CDW phase transitions, a close-up view on the specific heat anomalies presented in Fig. 4b reveals transition (i) from the orthorhombic parent-type to the q_{1ic} -type CDW state at $T_{1ic} = 305$ K via a second order jump-like anomaly, $\Delta C_p \simeq 1.5(2)$ $\text{J mol}^{-1}\text{K}^{-1}$, and

(ii) a first-order phase transition (FOT) from the q_{1ic} - to the q_{2c} -type CDW state at around $T_{2c} \simeq 272$ K is indicated by a peak-like anomaly. Considering the first order nature of the latter transition (ii) and associated latent heat, a standard evaluation of heat capacity data collected with a relaxation-type technique (as applied for Fig. 4b may yield erroneous results and, thus, an adapted slope analysis for heating and cooling curves across that specific heat anomaly has been applied as implemented for this specific purpose in the software of the PPMS heat capacity option). Specific heat data resulting from the slope analysis of one such heating-cooling cycle is displayed in Fig. 4c and reveals (within error bars imposed by thermal gradients) an essentially reversible nature of the nearly symmetric peak-shape anomaly when comparing the heating (dark blue) and cooling (light blue) data (results of additional cycles with varying initial temperatures are shown in Fig. S3b in SM [34]) with a very similar width (~ 266 – 276 K) as indicated by the above discussed electrical resistivity data. The observed thermal reversibility across this transition is, within error bar, consistent with the above mentioned almost perfectly reversible behavior of the electrical resistivity, but nonetheless unexpected in context with a first order nature of that phase transition. A quantitative evaluation of the FOT anomaly in Fig. 4c yields associated enthalpy and entropy changes, $\Delta H \sim 30(3)$ J/mol and $\Delta S \sim 0.11(1)$ $\text{J mol}^{-1}\text{K}^{-1}$, respectively.

Thermal expansion data of YNiC_2 , $\Delta l/l(T)$ as merged in Fig. 5a with data from capacitive dilatometry ($T < 310$ K) and pXRD ($T > 310$ K), feature the CDW phase transitions: (i) via changes of slopes at T_{1ic} , *i.e.* by the typical thermal expansion feature of a second order phase transition, and (ii) the transition at T_{2c} , via a pronounced step-like anomaly of $\Delta l/l(T)$, which is indicative of a first order transition.

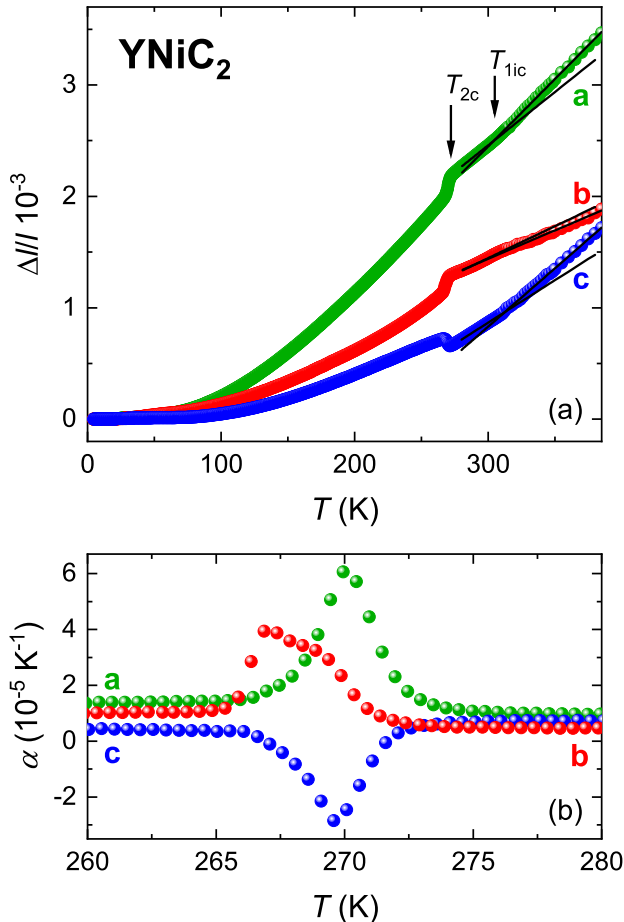


FIG. 5. (a) Temperature-dependent thermal expansion, $\Delta l/l(T)$, of YNiC_2 along orthorhombic a -, b - and c -orientations. Solid lines are guides to the eye for revealing approximate slope changes across T_{1ic} . (b) Expanded view of the thermal expansion coefficients at the q_{2c} -type CDW ordering temperature T_{2c} .

For both CDW transitions, the observed orientation dependent changes of the thermal expansion related to these phase transitions, when comparing signs of $\Delta l/l(T)$ anomalies along different orthorhombic orientations, imply reversed thermal shifts of the CDW phase transition upon stress or strain along these orientations (see below). At the second order CDW transition (i) at T_{1ic} , $\Delta l/l$ curves display rather subtle kink-like anomalies with an increase of slope upon increasing temperature for a - and c -axis data, but a decrease of slope for b -axis data. Experimental uncertainties caused by merging two different data sets right near transition (i) at T_{1ic} impede a quantitative evaluation of the changes of thermal expansion coefficients $\Delta\alpha$. At the first order CDW transition (ii) at T_{2c} , jump-like anomalies $\Delta l_a/l_a \simeq +1.5 \times 10^{-4}$ and $\Delta l_b/l_b \simeq +1.2 \times 10^{-4}$ are observed for orthorhombic a - and b -orientations, *i.e.* an expansion when raising temperature across the FOT, but on the contrary a length

contraction, $\Delta l_c/l_c \simeq -1.0 \times 10^{-4}$, which add up to a relative volume expansion, $\Delta V/V \sim +1.7 \times 10^{-4}$.

The initial response of the phase transition temperature T_{2c} to uni-axial pressure on YNiC_2 (assuming a constrained cross-section for the sake of simplicity) is evaluated via an adapted Clausius-Clapeyron relation, $dT_{2c}/d\sigma_i = (\Delta l/l_i)V_m/\Delta S \sim \Delta l/l_i \cdot 2.7 \times 10^{-4} \text{ K}\cdot\text{m}^2/\text{N}$, where σ_i is an uni-axial pressure along orientation i , $V_m = 2.92 \times 10^{-5} \text{ m}^3/\text{mol}$ is the molar volume of YNiC_2 and $\Delta S \sim 0.11(1) \text{ J mol}^{-1}\text{K}^{-1}$ is the above determined FOT entropy gain. The thermodynamic Clausius-Clapeyron relation, thus, yields an increase of T_{2c} upon uni-axial pressure along the orthorhombic a - and b -axis, *i.e.* $dT_{2c}/d\sigma_a \sim +4.1 \times 10^{-8} \text{ K}\cdot\text{m}^2/\text{N}$ (+41 K/GPa) and $dT_{2c}/d\sigma_b \sim +3.2 \times 10^{-8} \text{ K}\cdot\text{m}^2/\text{N}$ (+32 K/GPa) and, on the contrary, for uni-axial pressure along the orthorhombic c -axis a decrease $dT_{2c}/d\sigma_c \sim -2.7 \times 10^{-8} \text{ K}\cdot\text{m}^2/\text{N}$ (-27 K/GPa).

In course of the orthorhombic to monoclinic CDW phase transition, the formation of monoclinic twin-domains (see Sect. III A) in combination with the highly anisotropic length changes (see Fig. 5a) must obviously result in an evolution of local stress/strain patterns and, thus, in a local variation of T_{2c} . The latter results in a finite thermal width of the phase transition where q_{1ic} - and q_{2c} -type CDW domains coexist.

A close-up view in Fig. 5b on the anomalies of the thermal expansion coefficients $\alpha_i(T)$ across the phase transition at T_{2c} further reveals an unexpected shape of the anomaly of $\alpha_b(T)$. While those of $\alpha_a(T)$ and with reversed sign $\alpha_c(T)$ display a peak-shape similar to that of $C_p(T)$, the anomaly of $\alpha_b(T)$ exhibits a double peak-like maximum with the absolute maximum being substantially shifted towards the lower onset of the FOT. In the q_{2c} -type CDW state, for the sake of strain-energy minimization, a regular pattern of twin-domains is formed which is accompanied with an accordingly aligned pattern of stress and strain fields. With the disappearance of twin-domains across the transition into the q_{1ic} -type CDW state all stress and strain related to twin-formation will be relaxed and corresponding strain energy will be released. In addition, a lattice softening related to CDW sliding degrees of freedom may become relevant at the transition to the incommensurate q_{1ic} -type CDW state where translation symmetry is lost along the orthorhombic b -axis. Both aspects may thus contribute to some modifications of the thermal expansion anomalies as compared to the specific anomaly of the transition from the q_{1ic} - to q_{2c} -type CDW state. The strain effects are further relevant with respect to the observed, but unexpected, almost perfect thermally reversible behavior across the FOT at T_{2c} .

A reversible behavior at a first order structure phase transition results from a coupling mechanism which stabilizes specific phase ratios within a finite temperature interval as proposed earlier for a (similar to present case) orthorhombic to monoclinic ferroelectric transition in a hafnium-zirconium oxide film [46]. Local compres-

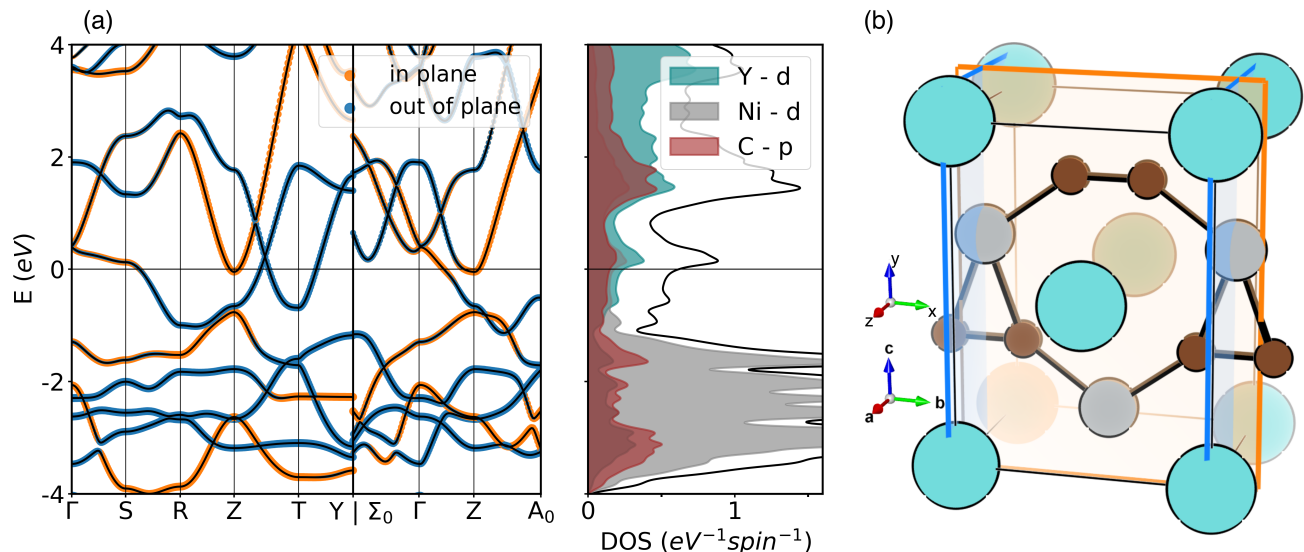


FIG. 6. (a) Electronic band structure and projected DOS in the orthorhombic type (a) parent state of YNiC_2 . The bands are colored with a linear combination of projections onto atomic orbitals. In particular, orange indicates the *in plane* combination, while blue indicates the *out of plane* combination, as defined in the text. (b) Sketch of the YNiC_2 crystal structure highlighting the *in plane* (orange) and *out of plane* (blue) directions.

sive stress evolving from the orthorhombic to monoclinic structure transformation was suggested to stabilize an orthorhombic phase fraction across a wide temperature interval. The orthorhombic to monoclinic CDW phase transition of YNiC_2 , as detailed in the previous paragraph, is well suited to originate local strain patterns which, in course of energy minimization, stabilize a mixed pattern of q_{1ic} -type and q_{2c} -type CDW domains within a finite temperature interval, *i.e.* within the width of the transition. A simultaneous appearance of corresponding q_{1ic} and q_{2c} satellite reflections at around 275 K was also confirmed by single crystal diffraction data discussed in Sect. III A.

Contrary to the single crystal case, anisotropic thermal expansion of grains in a polycrystal will cause inter-grain strain already upon cooling within the orthorhombic parent state and, indeed, CDW phase transitions of polycrystalline YNiC_2 extend over about twice as large temperature intervals (compare Ref. [39]). The nature of strain effects, originating from inter-grain strain as predetermined by thermal history in polycrystals versus energy minimizing orthorhombic to monoclinic phase coupling in monocrystals, is rather different and, thus, the suppression of hysteretic behavior expected to be less effective for polycrystals. The latter is supported by resistivity data of polycrystalline YNiC_2 reported in Ref. [39] and by a reference heat capacity measurement of polycrystalline YNiC_2 analogous to that in Fig. 4c, which however did not at all reproduce the essentially reversible behavior of the single crystal data (compare Figs. S3b and S3c in SM [34]).

D. DFT study of electronic and vibrational properties

To explain the origin of the experimental observations in terms of the electronic structure of YNiC_2 , we performed *ab initio* DFT calculations on the orthorhombic parent and distorted CDW phases. We note that all calculations were performed using the experimental structures, as reported in Sect. II, of course, except for the q_{1ic} -type CDW phase which lacks translation symmetry along the b -axis and is, thus, simplified to a 16-atoms approximant cell, in the following referred to as q_{1c} -type CDW. For further details we refer the interested reader to SM [34].

Figure 6a presents the electronic band structure of the orthorhombic CeNiC_2 structure-type parent phase of YNiC_2 , projected onto two different subsets of orbitals, that from here on we will name *in plane* (orange) and *out of plane* (blue). Their meaning is sketched in Fig. 6b. According to this definition, *in plane* orbitals are C and Ni orbitals lying mainly in the xy plane (orange plane in Fig. 6b), plus Y orbitals along the z direction. Complementarily, *out of plane* orbitals are C and Ni orbitals mainly in the z direction, and Y orbitals in the xy plane (blue planes in Fig. 6b). For a more detailed definition see Ref. [47].

The choice of this unusual partitioning is motivated by the direct observation of the Kohn-Sham wavefunctions near the Fermi energy (Sect. IV of SM [34]), as well as the Wannier functions derived from those bands. The bands colored with these projections are shown in Fig. 6a; these are well separated in the *in plane* and *out of plane* char-

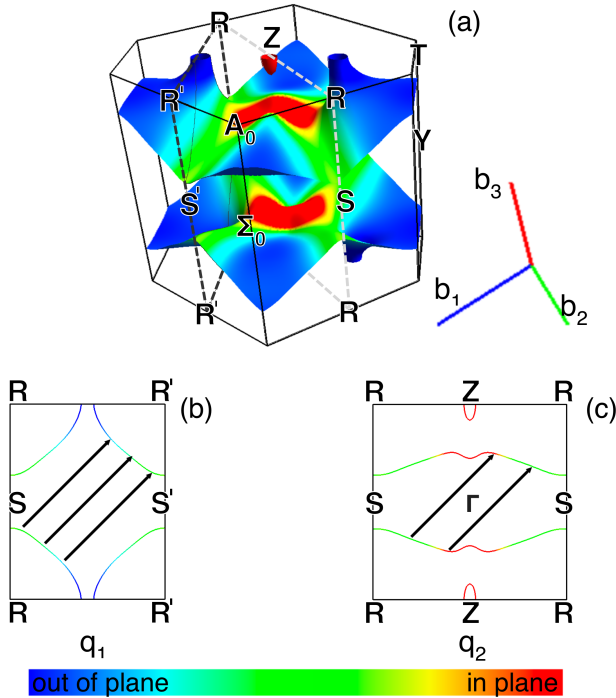


FIG. 7. (a) Fermi surface decorated with an *in plane* projection, cut with a plane (dashed lines) (b) and (c) 2D cuts indicating nesting vectors with q_1 and q_2 momentum, respectively.

acters, with the exception of a single band that changes character as it crosses the Fermi energy in the S–R and Γ –Z line. In addition to the bands, Fig. 6a shows the atom-projected density of states (DOS) where from -4 to -2 eV, the DOS exhibits mainly a Ni-*d* character, while in the -2 to 2 eV window around the Fermi energy the atomic character is evenly spread between Y, Ni, and C, consistent with the hybrid character of these states.

As we will discuss in the following, the change of band character is closely related to the CDW formation in YNiC₂. The Fermi energy is crossed by bands in the S–R and Γ –Z lines, and in Z–T and T–Y (see Fig. 6a). Resulting FS sheets are shown in Fig. 7a with a color scheme indicating an *in plane* projection of the character of electronic states. There are two different sheets: a main FS sheet formed by open quasi-1D sheets which are connected by hourglass-like pillars, and a small electron pocket centered around the Z point. The orbital character of the main FS sheet is extremely uneven, ranging from mainly *in plane* around the Γ –Z direction (red color), to mainly *out of plane* around Z–T and T–Y (blue color). It was pointed out earlier, that the strong quasi-1D character of the FS creates proper conditions for nesting with two primary *q*-vectors (*i.e.* q_1 and q_2) which can be revealed via FS contours obtained at proper 2D cuts of the Brillouin zone [48, 49]. Accordingly, we show in Fig. 7b and 7c two slices of the Brillouin zone hosting q_1 and q_2 nesting vectors, which in our *in plane* projection

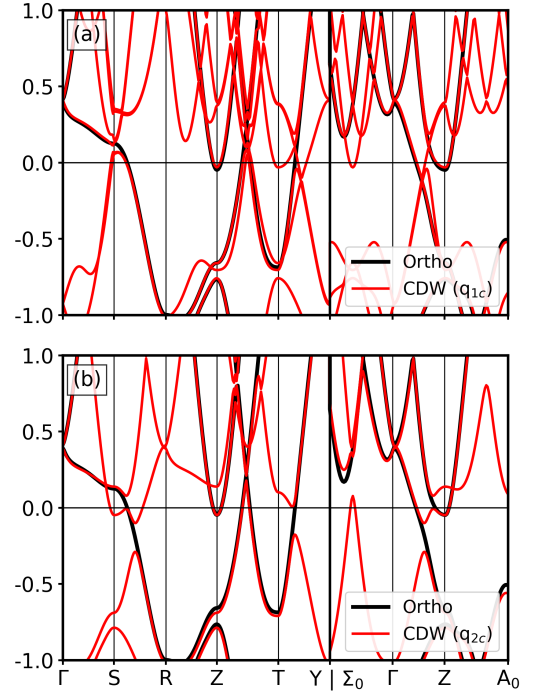


FIG. 8. Electronic band structure in q_{1c} -type (a) and q_{2c} -type (b) CDW state. The black line indicates the orthorhombic parent state, while the red line indicates the respective CDW phase.

connect states with *intermediate* (green-colored) character.

In order to investigate the impact of CDW formation on the electronic structure of YNiC₂, we directly compare the band structure of the orthorhombic parent phase with that of q_{1c} - and q_{2c} -type CDW phases in Fig. 8a and 8b, respectively, always following the paths in reciprocal space corresponding to the ones selected for the orthorhombic phase so that, folding aside, the bands lie on top of each other (see SM [34] Sect. II A for technical details). A common feature of both CDWs is that both open a gap in the Γ –Z and S–R lines, in correspondence to the region where the orbital character changes from *in plane* to *out of plane*. As a result, the only bands that previously changed character are now broken into two separate bands, each with its own well defined character. This separation of wave functions into bonding and antibonding states with distinctly distinguished *in plane* and *out of plane* character is highlighted in Fig. 9 via electron probability density plots as obtained from the Kohn-Sham wavefunction calculated for (a) the orthorhombic parent state and (b) the monoclinic q_{2c} -type CDW state (see also SM [34], Fig. S5 for projected band structures). This change of character is directly related to the direction of the atom displacements of the CDWs. Indeed, both are characterized mainly by the displacement of Ni in the *z* direction, *i.e.* out of the *xy* plane. This changes the hopping integrals, and lowers the energy of bands

with *out of plane* character, and raises the *in plane* ones, which lowers the total electronic energy as compared to the undistorted phase. While both CDWs feature certain similarities, it is clearly noticeable that the electronic structure modification caused by the q_{2c} -type CDW is much more pronounced: 150 meV large gaps open in the S–R, T–Y, and Γ –Z lines, while for the q_{1c} -type CDW the main gap opening is visible slightly above Fermi, and is of around 25 meV. This leads to a depletion of states in an energy window around the Fermi energy (see Fig. S6 and S7 in SM [34]), which is larger in the q_{2c} -type CDW state.

Figure 10 shows the Fermi surfaces decorated with a projection to *in plane* states for the orthorhombic parent (a), the q_{1c} - (b) and the q_{2c} -type (c) CDW states. In this perspective the separation of bands into *in plane* and *out of plane* character is even more evident, as CDW order splits the FS sheets into pockets of uniform character by removing a part of the quasi-planar sheets which connect them. This effect is already in action in the q_{1c} -type CDW, where a part of the quasi-1D sheet is already broken, and it further develops in the q_{2c} -type CDW state. Here, the FS becomes divided in a snake-like sheet connecting the pockets with *in plane* character (orange transparent box) and in the characteristic hourglass-shaped pillars with only *out of plane* character (azure transparent box), while an isolated pocket around the Z-point remains essentially unchanged.

Having examined the direct effect of the CDWs onto the electronic properties, we now move to establish its connection with the lattice dynamics. Figure 11 displays the phonon dispersions (a) calculated for the orthorhombic parent structure, along with the atom-projected phonon DOS (b) and the electron-phonon spectral function (c) and the nesting function ζ_0 (*i.e.* the static limit of the bare susceptibility) (d), calculated as defined in Ref. [41]. The latter quantity shows two broad, hump-shaped maxima located close to the points corresponding to the q_1 and q_2 vectors. The broadening is particularly pronounced in the vicinity to q_1 , where the maximum splits into two close peaks. The k -space shape of $\zeta_0(q)$ has previously been suggested to determine the presence or absence of CDW in early-lanthanide based $R\text{NiC}_2$ [48]. While sharp and well defined $\zeta_0(q)$ peaks at q_1 were found to promote this type of CDW in NdNiC_2 , GdNiC_2 and SmNiC_2 , the broadened features, reminiscent to those reported here for YNiC_2 , were seen in the case of LaNiC_2 , which shows no CDW order.

The phonon dispersions displayed in Fig. 11a present two dips: one at the R point (q_2), and one halfway between Z and A_0 (q_1). As highlighted by the thick red line around the dispersion, and the red curve below, in these two points we find the largest mode-resolved electron-phonon coupling $\lambda_{q,\mu=1}$. We note that the electron-phonon coupling is strongly anisotropic, and directly correlates with the orbital character (see SM [34], Fig. S8 for a direct comparison between the orbital character and the electron-phonon coupling) [50–52]. The two maxima

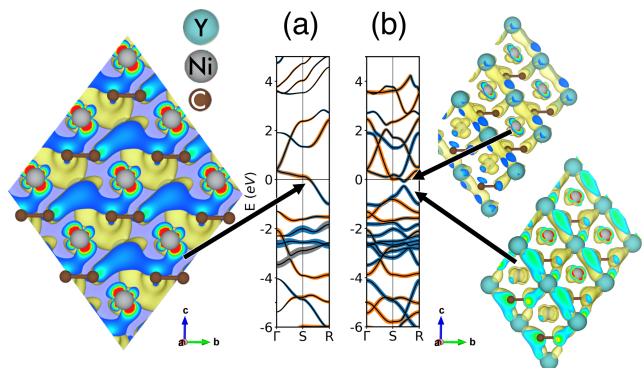


FIG. 9. Comparison of electronic bands along Γ –S–R lines, colored with a linear combination of projections onto atomic orbitals, in the orthorhombic parent phase (a) and the q_2 -type CDW phase (b). Aside, we show the probability density from the Kohn-Sham wavefunction at the wavevector and energy indicated with the black arrows.

of $\lambda_{q,\mu=1}$ ultimately dictate the CDW modulation vectors, rather than nesting alone, as argued in a general framework in Ref. [7].

These results allow us to confirm that the tendency to form both CDW phases is inherent to the orthorhombic parent phase. In addition, phonon calculations for the two CDW states (see SM [34], Fig. S9) reveal that the precursors of the q_{1c} -type CDW are present in the q_{2c} -type one, and vice versa. Qualitatively, the tendency of the q_{1c} -type CDW to form at higher temperature than the q_{2c} -type can be explained as a sort of intermediate phase which lowers the electronic energy less than the q_{2c} -type CDW phase, but with a higher electronic entropy gain.

IV. SUMMARY AND DISCUSSION

Shedding a light on the interplay between the competing electronic instabilities in $R\text{NiC}_2$ family has been a long-awaited step towards understanding the underlying physics. Such an opportunity has been opened by recent obtaining of high quality single crystals, allowing us for a direct and detailed exploration of the character and mechanisms of two CDW-types occurring in YNiC_2 probed by the combination of various experimental techniques with complementary theoretical calculations. The two types of CDW phases resolved for YNiC_2 , and characterized by wavevectors q_{1ic} and q_{2c} , leave distinct footprint in crystal and electronic structures and resulting experimental observables.

The q_1 -type CDW phase, appearing as the first CDW upon cooling from the orthorhombic parent state below T_{1ic} , weakly modifies the crystal structure producing a small incommensurate lattice modulation. The onset of this state opens a nearly isotropic electronic gap at Fermi energy. While a part of the high temperature FS is nested and removed, its overall character and topogra-

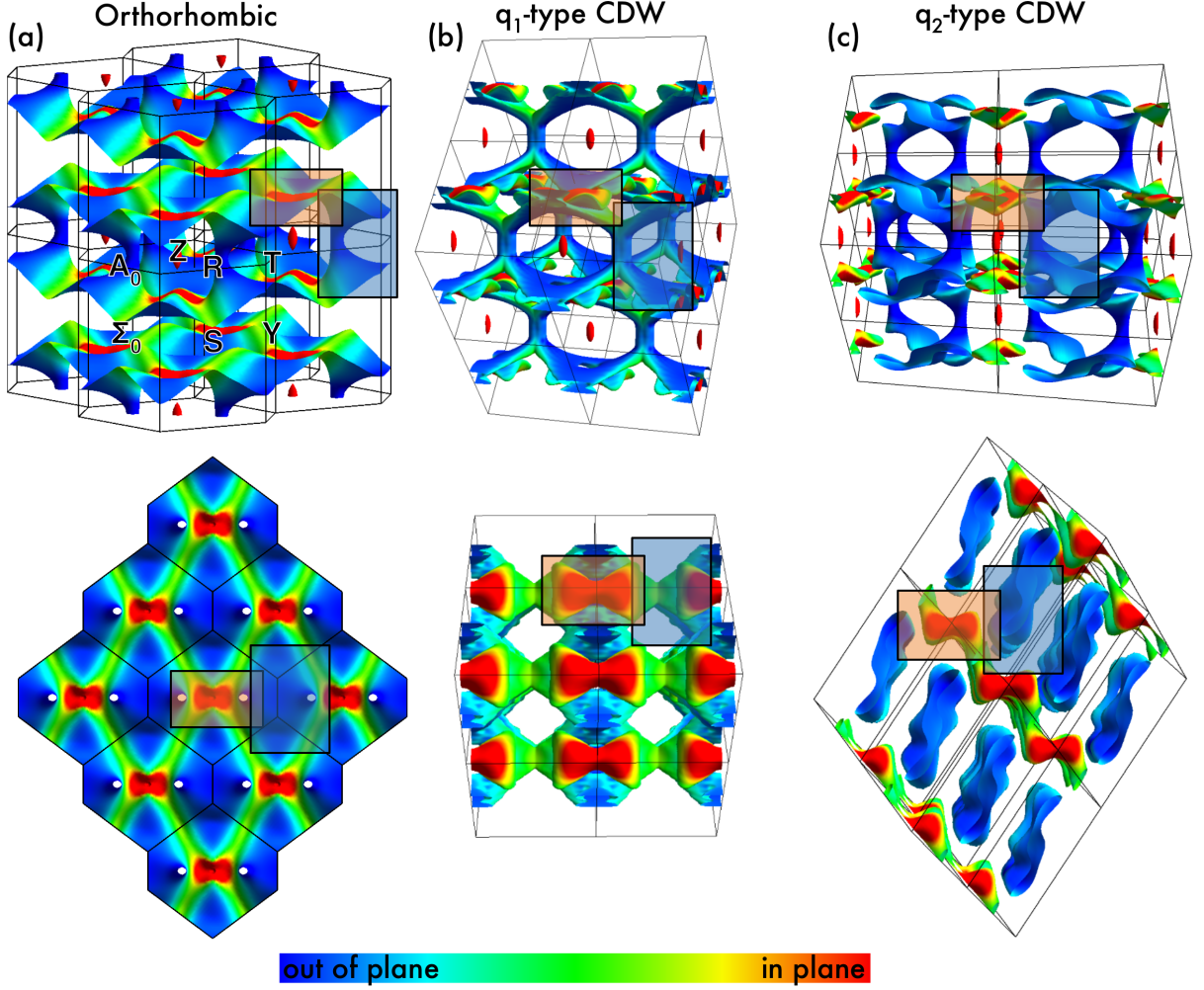


FIG. 10. Fermi surface with color-coded projection onto *in plane* states for (a) orthorhombic parent, (b) q_{1c} -type CDW, (c) q_{2c} -type CDW states with a side view perspective (top) and top view perspective (bottom). The orange and azure transparent boxes highlight common features of the FS in the different phases: a ribbon-like and an hourglass-like feature, respectively.

phy is mostly conserved. The quasi-planar FS sheets running perpendicular to a^* of the undistorted orthorhombic state, responsible for favoring the a direction in the terms of electrical resistivity, retain most of their area. For that reason, the ρ_b/ρ_a and ρ_c/ρ_a ratios, being the effective measure of transport anisotropy, remain rigid across the transition towards the q_{1c} -type CDW state.

The q_{2c} -type CDW, which prevails over the q_{1c} -type CDW phase at lower temperatures much more significantly modifies the properties of YNiC_2 . The crossover between the two CDW types leads to a large modification of the underlying crystal lattice, to the extent that it lowers the symmetry class from $Amm2$ to Cm . Moreover, the q_{2c} -type CDW state causes a more drastic FS decomposition. This process removes a large part of quasi-planar sheets, which in both, the orthorhombic undistorted and the q_{1c} -approximate CDW state, bridge the subsequent FS counterparts. As a consequence, FS in the q_{2c} -type CDW state is reduced to smaller, yet mul-

tiply, isolated pockets, predominantly with 3D character and dispersion in all three dimensions. This phenomenon is directly reflected by the suppression of electronic anisotropy as observed in transport properties. In particular, one can notice, that the thermal dependence of ρ_a experiences a pronounced upturn at T_{2c} , which is caused by removal of large FS part perpendicular to a^* . Simultaneously, $\rho_b(T)$ and $\rho_c(T)$ turn in the opposite direction, which is caused by the increased contribution of quasi-3D FS elements. Moreover, the contrast in the global influence on the electronic structure is demonstrated by the larger, as compared to the q_{1c} -approximate CDW state, decrease of DOS in the vicinity of the Fermi level, as shown in Fig. S7 of SM [34].

Although the impact on the FS differs significantly between the two CDW phases, there exists a common FS part, which is decomposed in each of them. This is further supported by the bare susceptibility ζ_0 , which was calculated within both states, q_{1c} - and q_{2c} -type (see

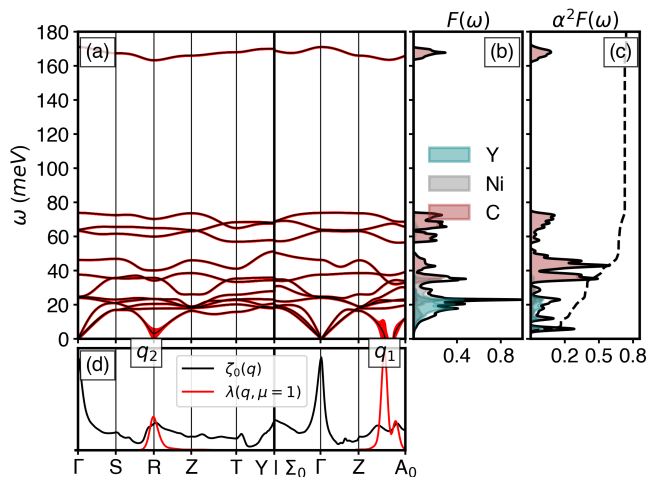


FIG. 11. Phonon dispersions (a), decorated with electron-phonon coupling (red thick line), atom-projected phonon DOS, $F(\omega)$ (b), and electron-phonon spectral function, $\alpha^2 F(\omega)$ (c), with integrated electron-phonon coupling. The projections onto Y, Ni, and C, are indicated as yellow, gray, and red shaded areas. (d) static limit of the bare susceptibility, ζ_0 , black line, and electron-phonon coupling for the first phonon mode, $\lambda(\mu = 1)$, red line.

Fig. S9 in SM [34]), and shows no clear peaks corresponding to the complementary CDW phase. The opening of a gap significantly reduces the potential for a secondary FS modification caused by nesting of that part which survives the first CDW transition. Therefore, YNiC_2 does not belong to the group of systems where the onset of a secondary density wave instability complements the FS decomposition already inflicted by the preexisting CDW, and removes its remaining components. Such an avalanche of two or three subsequent CDW instabilities has been reported in tungsten bronzes, where, in contrast to the case of YNiC_2 , the independent orders supplement each other and do not compete for the same FS spot [53, 54].

An intriguing observation stems from the comparison of the electron-phonon coupling parameter, λ , calculated in the q_{1c} -approximate and the q_{2c} -type CDW states, respectively. Within each of the two CDW states, $\lambda(q)$ shows distinct maxima corresponding to the alternative CDW modulation. In particular, within the q_{1c} -approximate CDW state, $\zeta_0(q)$ shows a weakly developed feature at $q \simeq q_2$, while a well-defined, sharp peak is seen in $\lambda(q)$ at the same q -position. This observation suggests, that momentum dependent electron-phonon coupling plays a decisive role in the first-order incommensurate to commensurate CDW phase transition occurring at T_{2c} . Moreover, also in the q_{2c} -type CDW state, one can notice a clear maximum of $\lambda(q)$ at q_1 . Interestingly, the signatures of such dormant adversary state precursors have already been observed in SmNiC_2 and GdNiC_2 compounds [21, 22]. In these materials, where only the q_{1c} -type CDW develops a long range order, a weak X-ray

diffuse scattering signal remains observable at the q_{2c} -position. Therefore, in YNiC_2 , and likely also in other intermediate members of the $R\text{NiC}_2$ series, small details may decide on the result of the competition between q_1 and q_2 lattice modulations. The suppression of one of these entities by internal or external factors, such as rare-earth magnetism, uni-axial pressure or strain, may give the other one a potential to take over.

V. CONCLUSIONS

We have explored physical properties of YNiC_2 , with particular emphasis on investigating the character, origin and consequences of the two charge density wave transitions observed in this compound. To obtain a detailed picture we have combined a number of different experimental techniques and theoretical methods, from single crystal diffraction, through thermal and transport studies to DFT calculations. Our analysis shows the contrasting effects of the two CDW states examined. The first transition near room temperature, from the undistorted orthorhombic CeNiC_2 -type parent structure towards the CDW state with modulation vector $q_{1ic} = (0.5, 0.5 + \eta, 0)$, only moderately impacts the electronic structure and related physical properties. The consequences of the second CDW transition to a state characterized by the modulation vector $q_{2c} = (0.5, 0.5, 0.5)$ are more pronounced. It not only changes the crystal structure by lowering the symmetry class and by generating larger atomic displacements, but also leads to a more significant FS decomposition, which is reflected in a considerably reduced anisotropy of transport properties. Both types of CDW instabilities are triggered by both FS nesting and momentum dependent electron-phonon coupling. This common thread, despite the large contrast in the microscopic and macroscopic consequences imposed by q_{1ic} - and q_{2c} -type CDW states, suggests that the balance between electronic and lattice degrees of freedom plays an important role in the competing interplay between them.

VI. ACKNOWLEDGMENTS

Financial support for M.R. by Grant No. BPN/BEK/2021/1/00245/DEC/1 of the Bekker Program of the Polish National Agency for Academic Exchange (NAWA) is gratefully acknowledged. S.D.C. acknowledges funding from the European Union - NextGenerationEU under the Italian Ministry of University and Research (MUR), “Network 4 Energy Sustainable Transition - NEST” project (MIUR project code PE000021, Concession Degree No. 1561 of Oct. 11, 2022) CUP C93C22005230007. Metallography support by Snezana Stojanovic and support with scanning electron microscopy and microprobe analysis by Monika Waas and Robert Svagera are gratefully acknowledged. S.D.C. likes to thank Lilia Boeri, Andriy Smolyanyuk and Martin Braß for the helpful dis-

cussion. The computational results presented have been

achieved using the Vienna Scientific Cluster (VSC).

-
- [1] G. Grüner, *Density Waves in Solids*, *Frontiers in Physics*, Vol. 89 (Addison-Wesley, New York, 1994).
- [2] G. Grüner, The dynamics of charge-density waves, *Rev. Mod. Phys.* **60**, 1129 (1988).
- [3] P. Monceau, Electronic crystals: an experimental overview, *Advances in Physics* **61**, 325 (2012).
- [4] X. Zhu, Y. Cao, J. Zhang, E. W. Plummer, and J. Guo, Classification of charge density waves based on their nature, *Proceedings of the National Academy of Sciences* **112**, 2367 (2015).
- [5] H.-M. Eiter, M. Lavagnini, R. Hackl, E. A. Nowadnick, A. F. Kemper, T. P. Devereaux, J.-H. Chu, J. G. Analytis, I. R. Fisher, and L. Degiorgi, Alternative route to charge density wave formation in multiband systems, *Proceedings of the National Academy of Sciences* **110**, 64 (2013).
- [6] J. Z. Xuetao Zhu, Jiandong Guo and E. W. Plummer, Misconceptions associated with the origin of charge density waves, *Advances in Physics: X* **2**, 622 (2017).
- [7] M. D. Johannes and I. I. Mazin, Fermi surface nesting and the origin of charge density waves in metals, *Phys. Rev. B* **77**, 165135 (2008).
- [8] J. G. Si, W. J. Lu, H. Y. Wu, H. Y. Lv, X. Liang, Q. J. Li, and Y. P. Sun, Origin of the multiple charge density wave order in 1T-VSe₂, *Phys. Rev. B* **101**, 235405 (2020).
- [9] Y. Bai, T. Jian, Z. Pan, J. Deng, X. Lin, C. Zhu, D. Huo, Z. Cheng, Y. Liu, P. Cui, Z. Zhang, Q. Zou, and C. Zhang, Realization of multiple charge-density waves in NbTe₂ at the monolayer limit, *Nano Letters* **23**, 2107 (2023).
- [10] J. Hwang, W. Ruan, Y. Chen, S. Tang, M. F. Crommie, Z.-X. Shen, and S.-K. Mo, Charge density waves in two-dimensional transition metal dichalcogenides, *Reports on Progress in Physics* **87**, 044502 (2024).
- [11] P. Foury-Leylekan, E. Sandré, S. Ravy, J.-P. Pouget, E. Elkaim, P. Roussel, D. Groult, and P. Labbé, Sliding charge density wave in the monophosphate tungsten bronze (PO₂)₄(WO₃)_{2m} with alternate stacking of $m = 4$ and $m = 6$ (WO₃) layers, *Phys. Rev. B* **66**, 075116 (2002).
- [12] C. D. Malliakas, M. Iavarone, J. Fedor, and M. G. Kanatzidis, Coexistence and coupling of two distinct charge density waves in Sm₂Te₅, *Journal of the American Chemical Society* **130**, 3310 (2008).
- [13] R. G. Moore, V. Brouet, R. He, D. H. Lu, N. Ru, J.-H. Chu, I. R. Fisher, and Z.-X. Shen, Fermi surface evolution across multiple charge density wave transitions in ErTe₃, *Phys. Rev. B* **81**, 073102 (2010).
- [14] B. F. Hu, B. Cheng, R. H. Yuan, T. Dong, and N. L. Wang, Coexistence and competition of multiple charge-density-wave orders in rare-earth tritellurides, *Phys. Rev. B* **90**, 085105 (2014).
- [15] L. Fu, A. M. Kraft, B. Sharma, M. Singh, P. Walmsley, I. R. Fisher, and M. C. Boyer, Multiple charge density wave states at the surface of TbTe₃, *Phys. Rev. B* **94**, 205101 (2016).
- [16] X. Teng, L. Chen, F. Ye, E. Rosenberg, Z. Liu, J.-X. Yin, Y.-X. Jiang, J. S. Oh, M. Z. Hasan, K. J. Neubauer, B. Gao, Y. Xie, M. Hashimoto, D. Lu, C. Jozwiak, A. Bostwick, E. Rotenberg, R. J. Birgeneau, J.-H. Chu, M. Yi, and P. Dai, Discovery of charge density wave in a kagome lattice antiferromagnet, *Nature* **609**, 490 (2022).
- [17] X. Teng, J. S. Oh, H. Tan, L. Chen, J. Huang, B. Gao, J.-X. Yin, J.-H. Chu, M. Hashimoto, D. Lu, C. Jozwiak, A. Bostwick, E. Rotenberg, G. E. Granroth, B. Yan, R. J. Birgeneau, P. Dai, and M. Yi, Magnetism and charge density wave order in kagome FeGe, *Nature Physics* **19**, 814 (2023).
- [18] S. Cao, C. Xu, H. Fukui, T. Manjo, Y. Dong, M. Shi, Y. Liu, C. Cao, and Y. Song, Competing charge-density wave instabilities in the kagome metal ScV₆Sn₆, *Nature Communications* **14**, 7671 (2023).
- [19] A. Kogar, A. Zong, P. E. Dolgirev, X. Shen, J. Straquadine, Y.-Q. Bie, X. Wang, T. Rohwer, I.-C. Tung, Y. Yang, R. Li, J. Yang, S. Weathersby, S. Park, M. E. Kozina, E. J. Sie, H. Wen, P. Jarillo-Herrero, I. R. Fisher, X. Wang, and N. Gedik, Light-induced charge density wave in LaTe₃, *Nature Physics* **16**, 159 (2020).
- [20] N. Yamamoto, R. Kondo, H. Maeda, and Y. Nogami, Interplay of Charge-Density Wave and Magnetic Order in Ternary Rare-Earth Nickel Carbides, RNiC₂ (R=Pr and Nd), *J. Phys. Soc. Jpn.* **82**, 123701 (2013).
- [21] S. Shimomura, C. Hayashi, G. Asaka, N. Wakabayashi, M. Mizumaki, and H. Onodera, Charge-density-wave destruction and ferromagnetic order in SmNiC₂, *Phys. Rev. Lett.* **102**, 076404 (2009).
- [22] S. Shimomura, C. Hayashi, N. Hanasaki, K. Ohnuma, Y. Kobayashi, H. Nakao, M. Mizumaki, and H. Onodera, Multiple charge density wave transitions in the antiferromagnets RNiC₂ (R= Gd, Tb), *Phys. Rev. B* **93**, 165108 (2016).
- [23] M. Roman, J. Strychalska-Nowak, T. Klimczuk, and K. K. Kolincio, Extended phase diagram of RNiC₂ family: Linear scaling of the peierls temperature, *Phys. Rev. B* **97**, 041103 (2018).
- [24] H. Maeda, R. Kondo, and Y. Nogami, Multiple charge density waves compete in ternary rare-earth nickel carbides, RNiC₂ (R: Y, Dy, Ho, and Er), *Phys. Rev. B* **100**, 104107 (2019).
- [25] M. Roman, M. Fritthum, B. Stöger, D. T. Adroja, and H. Michor, Charge density wave and crystalline electric field effects in TmNiC₂, *Phys. Rev. B* **107**, 125137 (2023).
- [26] S. Steiner, H. Michor, O. Sologub, B. Hinterleitner, F. Höfenstock, M. Waas, E. Bauer, B. Stöger, V. Babizhetskyy, V. Levytshkyy, and B. Kotur, Single-crystal study of the charge density wave metal LuNiC₂, *Phys. Rev. B* **97**, 205115 (2018).
- [27] STOE & Cie GmbH, X-Area 1.31.175.0, LANA 2.6.2.0 (2021).
- [28] V. Petříček, M. Dušek, and L. Palatinus, Crystallographic Computing System JANA2006: General features, *Z. Kristallogr.* **229**, 345 (2014).
- [29] Fachinformationszentrum Karlsruhe, Inorganic crystal structure database (ICSD) (2023).
- [30] M. Rotter, H. Müller, E. Gratz, M. Doerr, and M. Loewenhaupt, A miniature capacitance dilatometer

- for thermal expansion and magnetostriction, *Rev. Sci. Instrum.* **69**, 2742 (1998).
- [31] QUANTUM ESPRESSO: a modular and open-source software project for quantum simulations of materials, *Journal of Physics: Condensed Matter* **21**, 395502 (2009).
- [32] P. Giannozzi, O. Andreussi, T. Brumme, O. Bunau, M. B. Nardelli, M. Calandra, R. Car, C. Cavazzoni, D. Ceresoli, M. Cococcioni, N. Colonna, I. Carnimeo, A. D. Corso, S. de Gironcoli, P. Delugas, R. A. DiStasio, A. Ferretti, A. Floris, G. Fratesi, G. Fugallo, R. Gebauer, U. Gerstmann, F. Giustino, T. Gorni, J. Jia, M. Kawamura, H.-Y. Ko, A. Kokalj, E. Küçükbenli, M. Lazzeri, M. Marsili, N. Marzari, F. Mauri, N. L. Nguyen, H.-V. Nguyen, A. O. de-la Roza, L. Paulatto, S. Poncé, D. Rocca, R. Sabatini, B. Santra, M. Schlipf, A. P. Seitsonen, A. Smogunov, I. Timrov, T. Thonhauser, P. Umari, N. Vast, X. Wu, and S. Baroni, Advanced capabilities for materials modelling with quantum ESPRESSO, *J. Phys.: Condens. Matter* **29**, 465901 (2017).
- [33] D. R. Hamann, Optimized norm-conserving Vanderbilt pseudopotentials, *Phys. Rev. B* **88**, 085117 (2013).
- [34] See Supplemental Material at [URL will be inserted by publisher] for details of the computational methods, details of the lattice notation and CDW wavevectors, complementary experimental results and further details of the calculated electronic and phonon structures. SM contains also References [35-39].
- [35] A. P. Cracknell, B. L. Davies, S. C. Miller, and W. F. Love, *General introduction and tables of irreducible representations of space groups* (1979).
- [36] M. I. Aroyo, J. M. Perez-Mato, C. Capillas, E. Kroumova, S. Ivantchev, G. Madariaga, A. Kirov, and H. Wondratschek, Bilbao crystallographic server i: Databases and crystallographic computing programs, *Zeitschrift fuer Kristallographie* **221**, 15 (2006).
- [37] M. I. Aroyo, A. Kirov, C. Capillas, J. M. Perez-Mato, and H. Wondratschek, Bilbao crystallographic server ii: Representations of crystallographic point groups and space groups, *Acta Cryst.* **A62**, 115 (2006).
- [38] K. Momma and F. Izumi, VESTA: a three-dimensional visualization system for electronic and structural analysis, *Journal of Applied crystallography* **41**, 653 (2008).
- [39] K. K. Kolincio, M. Roman, and T. Klimczuk, Charge density wave and large nonsaturating magnetoresistance in YNiC_2 and LuNiC_2 , *Phys. Rev. B* **99**, 205127 (2019).
- [40] M. Kawamura, Fermisurfer: Fermi-surface viewer providing multiple representation schemes, *Computer Physics Communications* **239**, 197 (2019).
- [41] EPW: Electron-phonon coupling, transport and superconducting properties using maximally localized Wannier functions, *Comput. Phys. Commun.* **209**, 116 (2016).
- [42] H. Lee, S. Poncé, K. Bushick, S. Hajinazar, J. Lafente-Bartolome, J. Leveillee, C. Lian, J.-M. Lihm, F. Macheda, H. Mori, *et al.*, Electron-phonon physics from first principles using the epw code, *npj Computational Materials* **9**, 156 (2023).
- [43] T. Hahn and M. I. Aroyo, Symbols of symmetry elements, in *Space-group symmetry*, International Tables For Crystallography, Vol. A (IUCr, Chester, 2016) Chap. 2.1.2, pp. 144–148.
- [44] W. Jeitschko and M. Gerss, Ternary carbides of the rare earth and iron group metals with CeCoC_2 - and CeNiC_2 -type structure, *J. Less Common Metals* **116**, 147 (1986).
- [45] A. Wölfel, L. Li, S. Shimomura, H. Onodera, and S. van Smaalen, Commensurate charge-density wave with frustrated interchain coupling in SmNiC_2 , *Physical Review B* **82**, 054120 (2010).
- [46] Y. Zheng, T. Xin, J. Yang, Y. Zheng, Z. Gao, Y. Wang, Y. Xu, Y. Cheng, K. Du, D. Su, R. Shao, B. Zhou, Z. Yuan, Q. Zhong, C. Liu, R. Huang, X. Tang, C. Duan, S. Song, Z. Song, and H. Lyu, In-situ atomic-level observation of reversible first-order transition in $\text{Hf}_{0.5}\text{Zr}_{0.5}\text{O}_2$ ferroelectric film, in *2022 International Electron Devices Meeting (IEDM)* (2022) pp. 6.3.1–6.3.4.
- [47] In-plane: $C - p_x + C - p_y + \text{Ni} - d_{xy} + \text{Ni} - d_{x^2-y^2} + Y - d_{xz} + Y - d_{yz} + Y - d_{z^2}$, Out-of-plane: $C - p_z + \text{Ni} - d_{xz} + \text{Ni} - d_{yz} + \text{Ni} - d_{z^2} + Y - d_{xy} + Y - d_{x^2-y^2}$.
- [48] J. Laverock, T. D. Haynes, C. Urfeld, and S. B. Dugdale, Electronic structure of RNiC_2 (R = Sm, Gd, and Nd) intermetallic compounds, *Phys. Rev. B* **80**, 125111 (2009).
- [49] J. N. Kim, C. Lee, and J.-H. Shim, Chemical and hydrostatic pressure effect on charge density waves of SmNiC_2 , *New Journal of Physics* **15**, 123018 (2013).
- [50] J. An and W. Pickett, Superconductivity of MgB_2 : covalent bonds driven metallic, *Physical Review Letters* **86**, 4366 (2001).
- [51] C. Heil and L. Boeri, Influence of bonding on superconductivity in high-pressure hydrides, *Physical Review B* **92**, 060508 (2015).
- [52] C. Heil, S. Di Cataldo, G. B. Bachelet, and L. Boeri, Superconductivity in sodalite-like yttrium hydride clathrates, *Physical Review B* **99**, 220502 (2019).
- [53] E. Wang, M. Greenblatt, I. E.-I. Rachidi, E. Canadell, M.-H. Whangbo, and S. Vadlamannati, Electronic instabilities of the quasi-two-dimensional monophosphate tungsten bronze $\text{P}_4\text{W}_{12}\text{O}_{44}$, *Phys. Rev. B* **39**, 12969 (1989).
- [54] E. Canadell and M.-H. Whangbo, Charge-density-wave instabilities expected in monophosphate tungsten bronzes, *Phys. Rev. B* **43**, 1894 (1991).

Supplemental Material for: Competing charge density wave phases in YNiC₂

Marta Roman,^{1,2,*} Simone Di Cataldo,^{1,3} Berthold Stöger,⁴ Lisa Reisinger,¹ Emilie Morineau,¹ Kamil K. Kolincio,⁵ and Herwig Michor^{1,†}

¹*Institute of Solid State Physics, TU Wien, Wiedner Hauptstrasse 8-10, A-1040 Wien, Austria*

²*Institute of Physics and Applied Computer Science, Faculty of Applied Physics and Mathematics, Gdansk University of Technology, Narutowicza 11/12, 80-233 Gdansk, Poland*

³*Dipartimento di Fisica, Sapienza University of Rome, Piazzale Aldo Moro 5, 00185 Rome, Italy*

⁴*X-Ray Center, TU Wien, Getreidemarkt 9, A-1060 Wien, Austria*

⁵*Faculty of Applied Physics and Mathematics, Gdansk University of Technology, Narutowicza 11/12, 80-233 Gdansk, Poland*

I. COMPUTATIONAL DETAILS

All calculations were performed using Quantum ESPRESSO [1, 2] and EPW [3]. We employed Optimized Norm-Conserving Vanderbilt Pseudopotentials [4], using the Perdew-Burke-Ernzerhof approximation for the exchange correlation functional. We employed a cutoff of 80 Ry on the plane waves expansion.

- **Orthorhombic parent phase**, self-consistency was achieved employing a uniform $12 \times 12 \times 12$ Monkhorst-Pack mesh and a Methfessel-Paxton smearing of 0.02 Ry for Brillouin zone integration of the ground-state charge density. The density of states was calculated non-self-consistently over a $32 \times 32 \times 32$ grid, using the tetrahedron method for integration. Phonon properties were computed over a $4 \times 4 \times 4$ grid. Using EPW, they were then interpolated over a $32 \times 32 \times 32$ k grid for the calculation of the phonon selfenergy and the bare susceptibility. Wannierization was obtained from a non-self-consistent calculation over a $4 \times 4 \times 4$ k -grid, using an initial guess with 5 d orbitals centered on Ni, and three sp^2 orbitals centered in between the two carbon atoms. An outer window from -4 to 4 eV, and a frozen window from -0.8 to 1.3 eV were employed for disentanglement.
- **q_{1c} -type CDW phase**, self-consistency was achieved employing a uniform $12 \times 12 \times 12$ Monkhorst-Pack mesh and a Methfessel-Paxton smearing of 0.02 Ry for Brillouin zone integration of the ground-state charge density. The density of states was calculated non-self-consistently over a $24 \times 24 \times 24$ grid, using the tetrahedron method for integration.
- **q_{2c} -type CDW phase**, self-consistency was achieved employing a uniform $4 \times 4 \times 4$ Monkhorst-Pack mesh and a Methfessel-Paxton smearing of 0.04 Ry for Brillouin zone integration of the ground-state charge density. The density of states was calculated non-self-consistently over a $24 \times 24 \times 24$ grid, using the tetrahedron method for integration.

II. DETAILS ON THE LATTICE NOTATION AND CDW WAVEVECTORS

In this section we clarify the settings employed in our calculations to describe coordinates and crystal structures.

A. Transformation from $Amm2$ to $Cm2m$

In the literature, $RNiC_2$ in the orthorhombic phase are often described in terms of their *conventional* cell in the $Amm2$ setting ($a < b < c$), i.e. with $a = 3.57$ Å, $b = 4.51$ Å, and $c = 6.03$ Å. **Note:** in the rest of this section and throughout the paper, a , b , and c remain fixed to these values.

Despite the $Amm2$ setting is often adopted in the experimental literature, we chose to employ the $Cm2m$ setting, following the notation of Cracknell *et al.* [5] and employed in the Bilbao Crystallographic Server [6, 7].

* marta.roman@pg.edu.pl

† michor@ifp.tuwien.ac.at

In this setting, the lattice vectors take the form:

$$\mathcal{A}_{Amm2}^p = \begin{bmatrix} \vec{a}_1 \\ \vec{a}_2 \\ \vec{a}_3 \end{bmatrix} = \begin{pmatrix} a/2 & -b/2 & 0 \\ a/2 & b/2 & 0 \\ 0 & 0 & c \end{pmatrix} \quad (1)$$

$$\mathcal{A}_{Cm2m}^p = \begin{bmatrix} \vec{a}_1 \\ \vec{a}_2 \\ \vec{a}_3 \end{bmatrix} = \begin{pmatrix} b/2 & -c/2 & 0 \\ b/2 & c/2 & 0 \\ 0 & 0 & a \end{pmatrix} \quad (2)$$

The corresponding reciprocal lattice vectors are given by (\mathcal{A} and \mathcal{B} denote matrices for direct and reciprocal lattices, respectively, the apex p denotes that these refer to the *primitive* lattice vectors):

$$\mathcal{B}_{Amm2}^p = \begin{bmatrix} \vec{b}_1 \\ \vec{b}_2 \\ \vec{b}_3 \end{bmatrix} = 2\pi \begin{pmatrix} 1/a & 1/a & 0 \\ -1/b & 1/b & 0 \\ 0 & 0 & 1/c \end{pmatrix} \quad (3)$$

$$\mathcal{B}_{Cm2m}^p = \begin{bmatrix} \vec{b}_1 \\ \vec{b}_2 \\ \vec{b}_3 \end{bmatrix} = 2\pi \begin{pmatrix} 1/b & 1/b & 0 \\ -1/c & 1/c & 0 \\ 0 & 0 & 1/a \end{pmatrix} \quad (4)$$

Given the matrix:

$$\mathcal{R} = \begin{pmatrix} 0 & 1 & 0 \\ 0 & 0 & 1 \\ 1 & 0 & 0 \end{pmatrix} \quad (5)$$

and the transform matrix \mathcal{T} from conventional \mathcal{B}_{Amm2}^c to primitive \mathcal{B}_{Amm2}^p :

$$\mathcal{T} = \begin{pmatrix} 1 & -1 & 0 \\ 1 & 1 & 0 \\ 0 & 0 & 1 \end{pmatrix} \quad (6)$$

one can write the corresponding wavevectors in the primitive $Cm2m$ setting as:

$$\mathcal{B}_{Cm2m}^p = \mathcal{T} \cdot \mathcal{R} \cdot \mathcal{B}_{Amm2}^c \cdot \mathcal{R}^{-1} \quad (7)$$

The usual definition of $q_{1c} = (0.50, 0.50, 0.00)$ and $q_{2c} = (0.50, 0.50, 0.50)$ refers to the *conventional* cell in $Amm2$ setting. As atomic coordinates are contravariant with respect to a change of basis, these wavevectors in the primitive $Cm2m$ cell are:

$$\vec{q}_{Cm2m}^p = \mathcal{R} \cdot \vec{q}_{Amm2}^c \cdot \mathcal{R}^{-1} \cdot \mathcal{T}^{-1} \quad (8)$$

From which we obtain the relations in the primitive, $Cm2m$ cell.

$$\begin{aligned} \vec{q}_{1c} &= (0.25, 0.25, 0.50) \\ \vec{q}_{2c} &= (0.50, 0.00, 0.50) \end{aligned} \quad (9)$$

B. Matching q_{1c}/q_{2c} and orthorhombic axes

In this section we report the lattice vectors and the coordinates of the special points for the q_{1c} and q_{2c} phases, as well as a technical discussion on how to employ them. The coordinates employed are summarized in Tab. II.

These coordinates can be obtained from the transform matrix \mathcal{T} between the orthorhombic and the q_{1c} and q_{2c} lattice vectors, following precisely the same procedure described in Sect. II. However, there is a technical difficulty that has to be taken care of. Density Functional Theory codes, as well as programs for structure visualization (e.g. VESTA [8]) will define lattice vectors following a certain convention, which effectively imposes a rotation of the Cartesian frame of reference in which the crystal is defined. In order for the procedure described in Sect. II to work, one has to first

establish a common frame of reference between the two crystals, and explicitly enforce the choice of lattice vectors so that the "real space" crystal described by them is oriented in the same way. Since, to the best of our knowledge, it is not possible to enforce this *a priori*, we developed a python script to rotate the frame of reference of the q_{1c}/q_{2c} crystal axes until all the atoms matched the parent phase within a certain distance threshold.

The crystal axes and atomic coordinates for the q_{1c} and q_{2c} phases employed in this work are

$$\mathcal{A}_{q_{1c}} = \begin{bmatrix} \vec{a}_1 \\ \vec{a}_2 \\ \vec{a}_3 \end{bmatrix} = \begin{pmatrix} -4.524 & 0.000 & -3.548 \\ 4.489 & 0.035 & -3.592 \\ 0.023 & -6.027 & -0.030 \end{pmatrix} \quad (10)$$

Atom	x	y	z
Y	0.000	0.000	0.000
Y	0.246	0.754	0.500
Y	0.496	0.504	0.003
Y	0.750	0.250	0.503
Ni	0.253	0.257	0.613
Ni	0.993	0.497	0.113
Ni	0.503	0.007	0.113
Ni	0.743	0.747	0.613
C	0.071	0.425	0.802
C	0.175	0.330	0.302
C	0.670	0.825	0.302
C	0.575	0.929	0.802
C	0.824	0.678	0.302
C	0.421	0.076	0.802
C	0.924	0.578	0.802
C	0.322	0.176	0.302

$$\mathcal{A}_{q_{2c}} = \begin{bmatrix} \vec{a}_1 \\ \vec{a}_2 \\ \vec{a}_3 \end{bmatrix} = \begin{pmatrix} 3.763 & 0.000 & 0.000 \\ -1.068 & 3.606 & -3.569 \\ -1.068 & 3.606 & 3.569 \end{pmatrix} \quad (11)$$

Atom	x	y	z
Y	0.005	0.505	0.505
Y	0.995	0.995	0.995
Ni	0.390	0.066	0.547
Ni	0.390	0.547	0.066
C	0.549	0.830	0.322
C	0.549	0.322	0.830
C	0.851	0.977	0.474
C	0.851	0.474	0.977

TABLE I. Atomic positions for q_{2c} in crystal coordinates

q_{1c}		q_{2c}	
Label	Coordinates	Label	Coordinates
Γ	(0.00,0.00,0.00)	Γ	(0.00,0.00,0.00)
S	(-0.50,0.50,-0.50)	S	(-0.05,0.51,0.51)
R	(-1.00,0.00,-0.50)	R	(-0.05,0.01,1.01)
Z	(-0.50,-0.50,0.00)	Z	(0.00,-0.50,0.50)
T	(-0.50,-0.50,-1.00)	T	(-0.53,-0.04,0.96)
Y	(0.00,0.00,-1.00)	Y	(-0.53,0.46,0.46)
Σ_0	(-0.78,0.78,0.00)	Σ_0	(0.34,0.43,0.43)
Γ	(0.00,0.00,0.00)	Γ	(0.00,0.00,0.00)
Z	(-0.50,-0.50,0.00)	Z	(0.00,-0.50,0.50)
A_0	(-1.28,0.27,0.00)	A_0	(0.34,-0.07,0.93)

TABLE II. Coordinates of the special points for the q_{1c} and q_{2c} phases employed in the band structure and phonon calculations

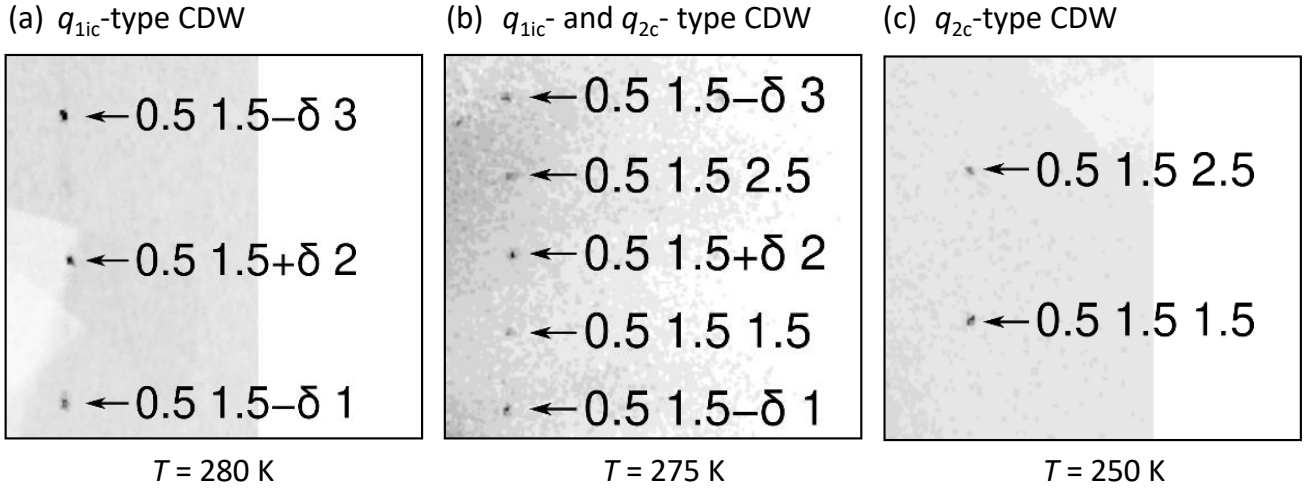


FIG. S1. $k = 1.5$ reciprocal space sections reconstructed from intensity data of a crystal in (a) the q_{1ic} -type CDW state, (b) both, the q_{1ic} -type and the q_2 -type CDW states, and (c) only the q_2 -type CDW state. Reflection indices are given with respect to the orthorhombic non-modulated structure.

III. COMPLEMENTARY EXPERIMENTAL RESULTS

A. Details of CDW phase transitions

In order to probe for thermal hysteresis across the two CDW phase transitions as accurate as possible, we measured the electrical resistivity with a YNiC_2 single crystal bar cut along the orthorhombic c -axis (see results in Fig.S2). The crystal was mounted on the PPMS rotator-insert with a metal plate sample holder where the sample is glued with GE-varnish. For electrical insulation, a thin cigarette paper is placed in between sample and the metal plate which is directly touching the calibrated CERNOX temperature sensor of the PPMS rotator-insert, thus insuring closest thermal contact between the sample and the temperature sensor. For a reliable thermalisation, the temperature was fully stabilized for each measurement point, with an average speed of temperature variation of 0.15 K/min in the T -range from 280 to 320 K and below 264 K, but as slow as 41 mK/min within the T -interval from 264 to 280 K. At the second-order phase transition near room temperature warming and cooling data match within the noise error of the measurement, whereas from data right at the first-order transition at around 272 K a very small but nonetheless finite hysteresis of the order of 0.1 K is revealed (see magnifying inserts in Fig.S2).

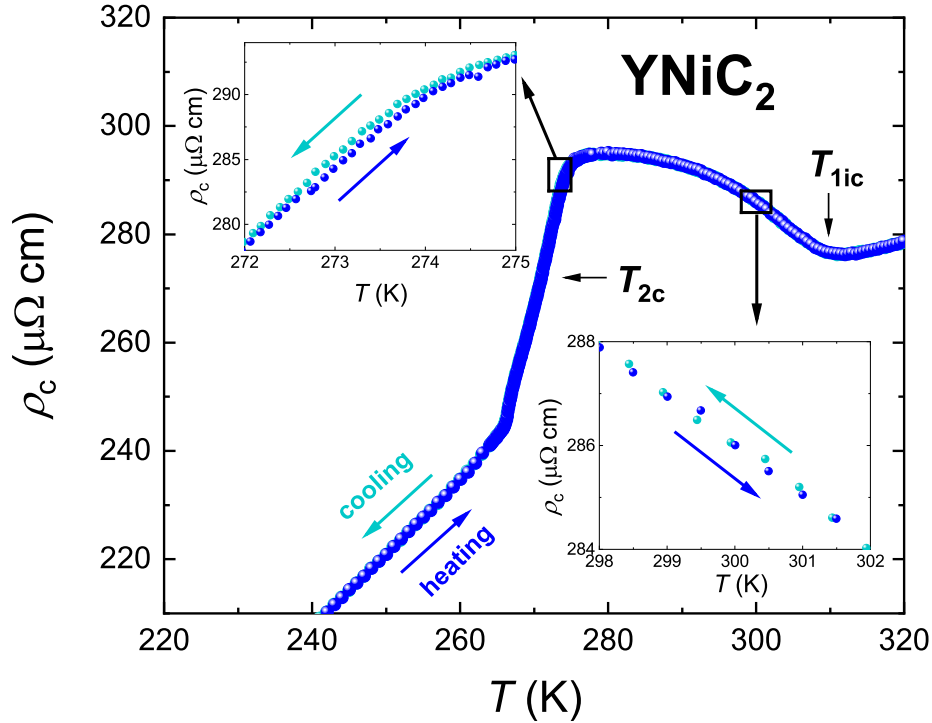


FIG. S2. High-temperature-resolution measurement of YNiC_2 electrical resistivity data, $\rho_c(T)$, measured across the second-order and first-order CDW phase transitions at T_{1ic} and T_{2c} , respectively, with initial cooling and subsequent heating.

B. Analysis of low temperature specific heat data

The specific heat of YNiC_2 at temperatures below 10 K is shown as C/T vs. T^2 plot in Fig. S4 and analyzed using the formula,

$$\frac{C_p}{T} = \gamma + \beta T^2, \quad (12)$$

where the first and second terms in the right side of eq. 12 represent the electronic and lattice contributions according to the basic Sommerfeld and Debye models, respectively, yielding a Sommerfeld coefficient $\gamma = 1.53 \text{ mJ mol}^{-1} \text{ K}^{-2}$ and Debye coefficient $\beta = 0.03936 \text{ mJ mol}^{-1} \text{ K}^{-4}$. The latter corresponds to a Debye temperature $\theta_D = 582 \text{ K}$ according to $\theta_D = \left(\frac{12\pi^4}{5\beta} nR\right)^{\frac{1}{3}}$ where $R = 8.314 \text{ mol}^{-1} \text{ K}^{-1}$ and n is the number of atoms per formula unit (here $n = 4$ for YNiC_2).

The estimated value of Sommerfeld coefficient matches well with the value $\gamma = 1.67 \text{ mJ mol}^{-1} \text{ K}^{-2}$ determined for polycrystalline representative [9]. On the other hand, it is slightly larger than $\gamma = 0.83 \text{ mJ mol}^{-1} \text{ K}^{-2}$ for the single-crystalline LuNiC_2 , also hosting q_{2c} -type CDW [10] suggesting that electronic structure of YNiC_2 is possibly less affected by the q_{2c} -type CDW formation.

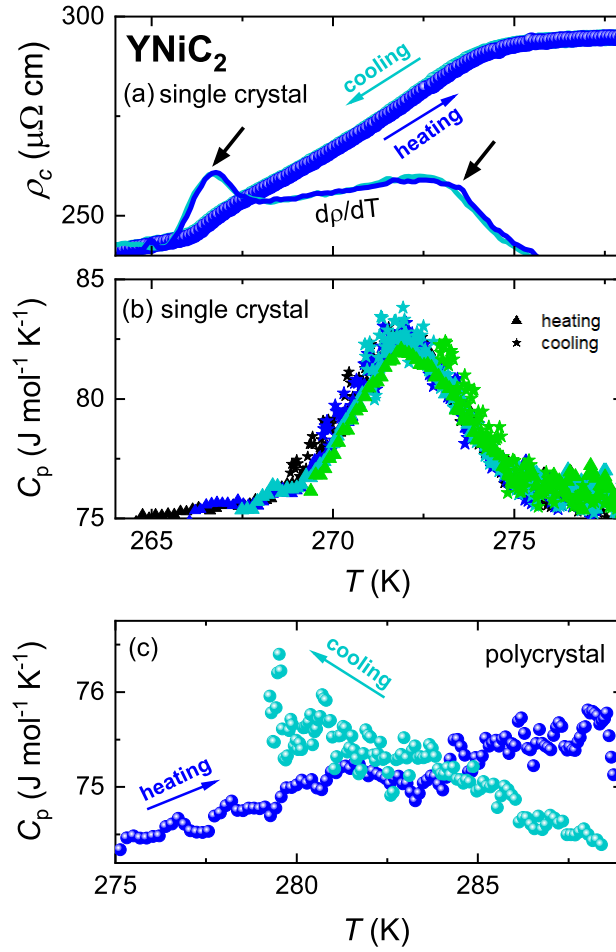


FIG. S3. Vicinity of the first order CDW phase transition at T_{2c} in: a) electrical resistivity measured c-direction b) Specific heat anomaly related to the first order CDW transition at T_{2c} as determined via a slope analysis of heating (triangle) and subsequent cooling (star) curves where different symbol colors refer to different starting temperatures of the pulses. c) Specific heat anomaly of polycrystalline YNiC_2 related to the (further broadened) first order CDW transition at around T_{2c} as determined via a slope analysis of heating (dark blue) and subsequent cooling (light blue) curves.

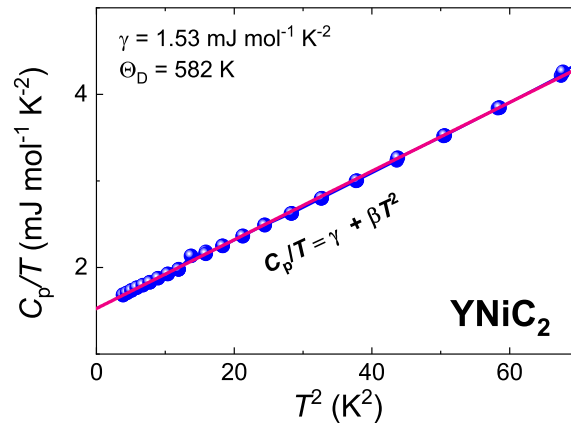


FIG. S4. C_p/T vs. T^2 where the pink solid line represents a $C_p/T = \gamma + \beta T^2$ fit.

IV. DETAILS OF ELECTRONIC PROPERTIES

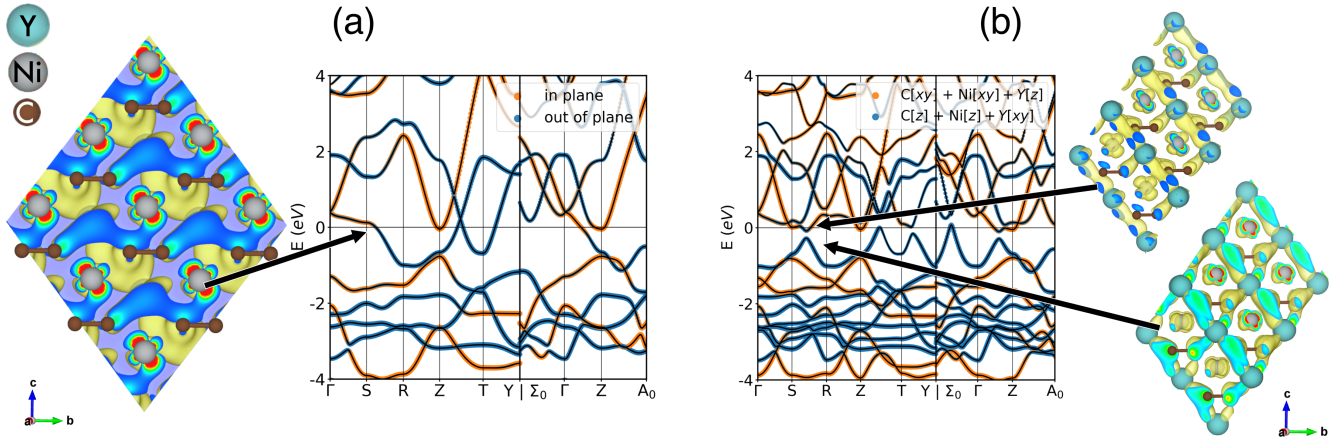


FIG. S5. Comparison between the electronic band structure in the orthorhombic parent phase (a) and in the distorted q_2 -type CDW phase (b). In the images, we show the probability density from the Kohn-Sham wavefunction at the wavevector and energy indicated with the black arrows.

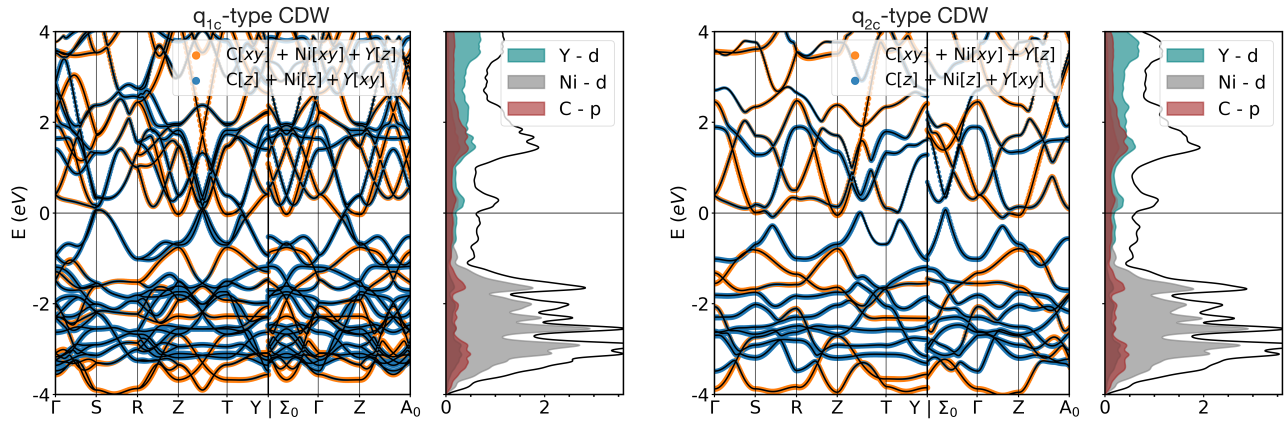


FIG. S6. Electronic band structure for the q_{1c} -type (left) and q_{2c} -type (right) CDW phases. The bands are colored with the *in plane* and *out of plane* combination, as defined in the main text.

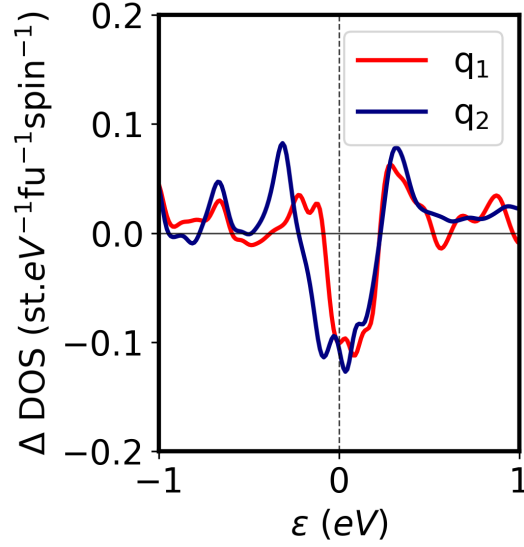


FIG. S7. Difference between the DOS of (in red) the q_{1c} - and (in blue) q_{2c} -type CDW phases with respect to the orthorhombic parent phase.

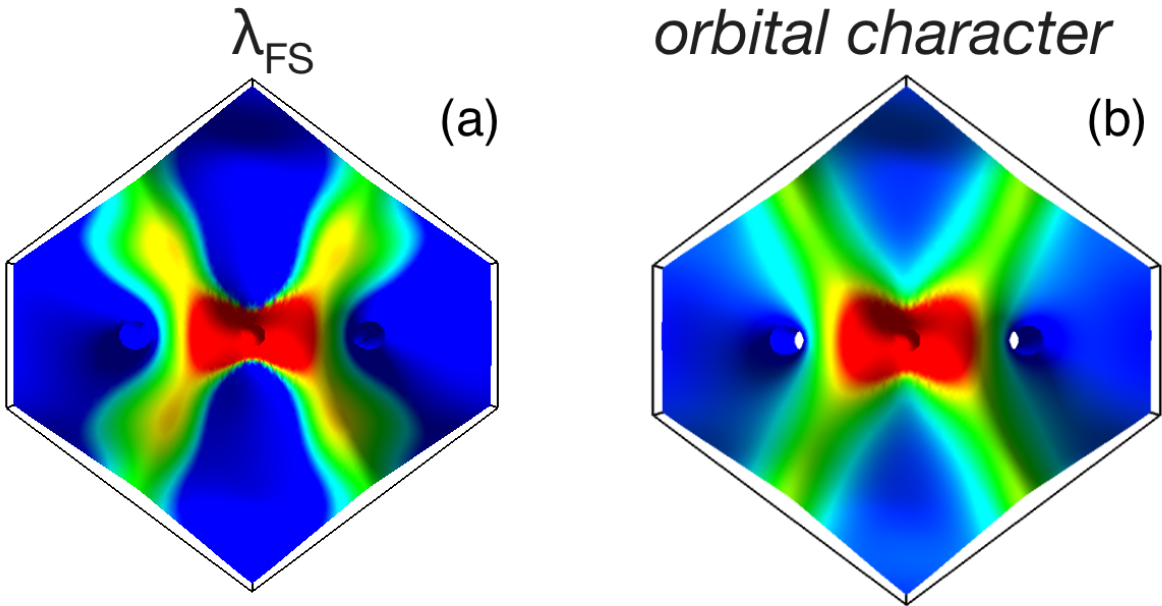


FIG. S8. Top view comparison of the Fermi surface of the orthorhombic parent phase of YNiC_2 decorated with the anisotropic electron-phonon coupling λ_q (a) and with the projection onto *in plane* states (see main text for the definition) (b). The range of the color scale in (a) from blue to red corresponds to values between 0.28 and 0.35 for the coupling, and a range from *out of plane* to *in-plane* for the orbital projection in (b).

V. DETAILS OF PHONON PROPERTIES

In this section we show the phonon dispersions of the q_{1c} -type (left) and q_{2c} -type (right) CDW phases, calculated from the phonon selfenergy within EPW [3, 11]. In the bottom panel, we report the static limit of the bare susceptibility along the same path. We note that in the q_{1c} phase, the instability relative to the q_{2c} phase is visible, and vice versa. Note that in the q_{1c} the Γ point of the parent cell is folded between Z and A_0 .

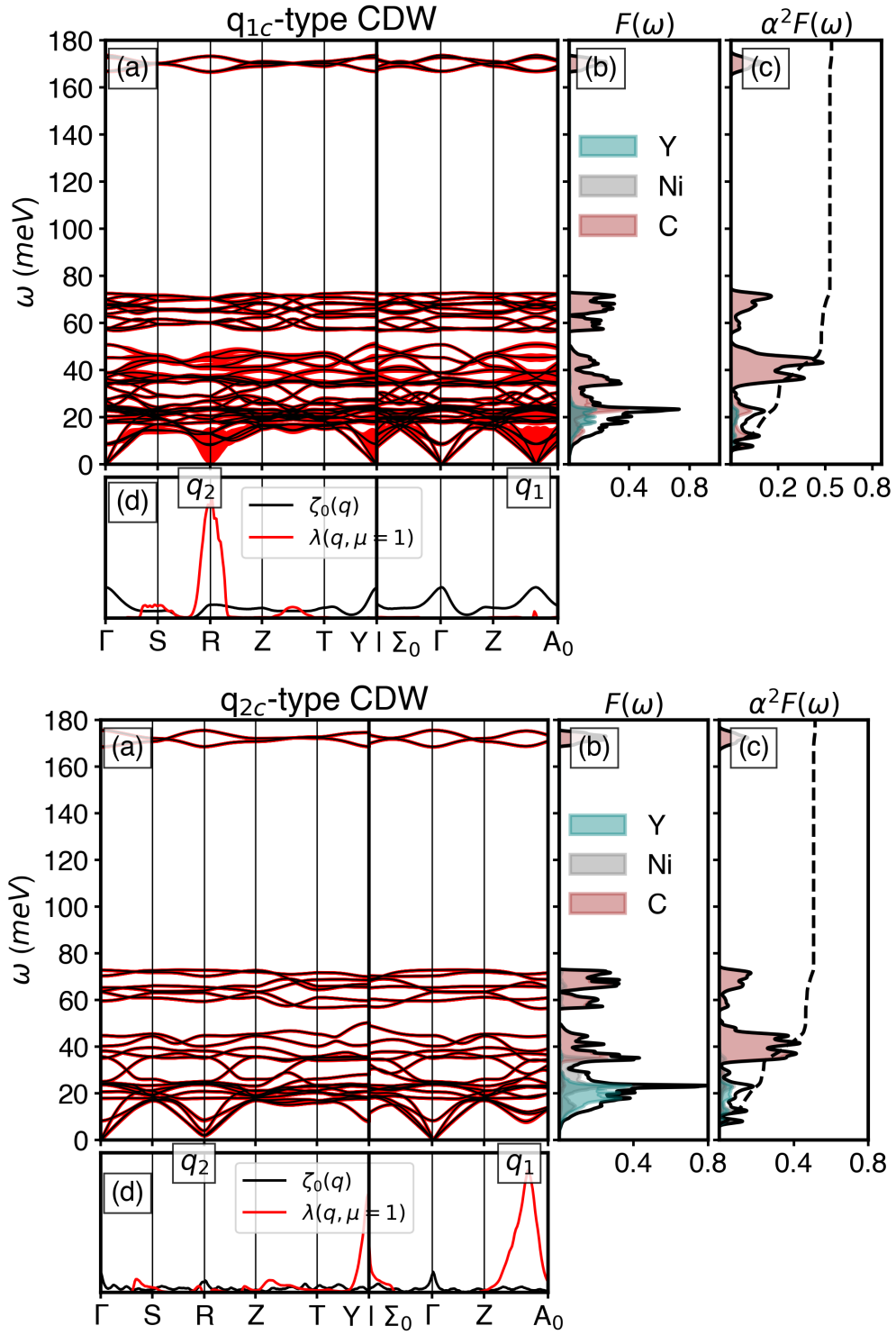


FIG. S9. Phonon dispersion (a), atom-projected phonon density of states, $F(\omega)$, (b), Eliashberg function, $\alpha^2F(\omega)$, (c) and nesting function (d) for the q_{1c} -type (upper) and q_{2c} -type (lower) CDW phases. The projections onto Y, Ni, and C are indicated as yellow, grey, and red shaded areas, respectively.

-
- [1] QUANTUM ESPRESSO: a modular and open-source software project for quantum simulations of materials, *Journal of Physics: Condensed Matter* **21**, 395502 (2009).
 - [2] P. Giannozzi, O. Andreussi, T. Brumme, O. Bunau, M. B. Nardelli, M. Calandra, R. Car, C. Cavazzoni, D. Ceresoli, M. Cococcioni, N. Colonna, I. Carnimeo, A. D. Corso, S. de Gironcoli, P. Delugas, R. A. DiStasio, A. Ferretti, A. Floris, G. Fratesi, G. Fugallo, R. Gebauer, U. Gerstmann, F. Giustino, T. Gorni, J. Jia, M. Kawamura, H.-Y. Ko, A. Kokalj, E. Küçükbenli, M. Lazzeri, M. Marsili, N. Marzari, F. Mauri, N. L. Nguyen, H.-V. Nguyen, A. O. de-la Roza, L. Paulatto, S. Poncé, D. Rocca, R. Sabatini, B. Santra, M. Schlipf, A. P. Seitsonen, A. Smogunov, I. Timrov, T. Thonhauser, P. Umari, N. Vast, X. Wu, and S. Baroni, Advanced capabilities for materials modelling with quantum ESPRESSO, *J. Phys.: Condens. Matter* **29**, 465901 (2017).
 - [3] EPW: Electron–phonon coupling, transport and superconducting properties using maximally localized Wannier functions, *Comput. Phys. Commun.* **209**, 116 (2016).
 - [4] D. R. Hamann, Optimized norm-conserving Vanderbilt pseudopotentials, *Phys. Rev. B* **88**, 085117 (2013).
 - [5] A. P. Cracknell, B. L. Davies, S. C. Miller, and W. F. Love, *General introduction and tables of irreducible representations of space groups* (1979).
 - [6] M. I. Aroyo, J. M. Perez-Mato, C. Capillas, E. Kroumova, S. Ivantchev, G. Madariaga, A. Kirov, and H. Wondratschek, Bilbao crystallographic server i: Databases and crystallographic computing programs, *Zeitschrift fuer Kristallographie* **221**, 15 (2006).
 - [7] M. I. Aroyo, A. Kirov, C. Capillas, J. M. Perez-Mato, and H. Wondratschek, Bilbao crystallographic server ii: Representations of crystallographic point groups and space groups, *Acta Cryst.* **A62**, 115 (2006).
 - [8] K. Momma and F. Izumi, VESTA: a three-dimensional visualization system for electronic and structural analysis, *Journal of Applied crystallography* **41**, 653 (2008).
 - [9] K. K. Kolincio, M. Roman, and T. Klimczuk, Charge density wave and large nonsaturating magnetoresistance in YNiC_2 and LuNiC_2 , *Phys. Rev. B* **99**, 205127 (2019).
 - [10] S. Steiner, H. Michor, O. Sologub, B. Hinterleitner, F. Höfenstock, M. Waas, E. Bauer, B. Stöger, V. Babizhetskyy, V. Levyt'skyy, and B. Kotur, Single-crystal study of the charge density wave metal LuNiC_2 , *Phys. Rev. B* **97**, 205115 (2018).
 - [11] H. Lee, S. Poncé, K. Bushick, S. Hajinazar, J. Lafuente-Bartolome, J. Leveillee, C. Lian, J.-M. Lihm, F. Macheda, H. Mori, *et al.*, Electron–phonon physics from first principles using the epw code, *npj Computational Materials* **9**, 156 (2023).